

San Jose State University
SJSU ScholarWorks

Master's Theses

Master's Theses and Graduate Research

2008

Design flow approach from inductors to antenna at PCB level

Joseph C. Chung
San Jose State University

Follow this and additional works at: https://scholarworks.sjsu.edu/etd_theses

Recommended Citation

Chung, Joseph C., "Design flow approach from inductors to antenna at PCB level" (2008). *Master's Theses*. 3521.
DOI: <https://doi.org/10.31979/etd.gx7n-dygs>
https://scholarworks.sjsu.edu/etd_theses/3521

This Thesis is brought to you for free and open access by the Master's Theses and Graduate Research at SJSU ScholarWorks. It has been accepted for inclusion in Master's Theses by an authorized administrator of SJSU ScholarWorks. For more information, please contact scholarworks@sjsu.edu.

DESIGN FLOW APPROACH FROM INDUCTORS TO ANTENNA AT PCB
LEVEL

A Thesis

Presented to

The Faculty of the Department of Electrical Engineering

San Jose State University

In Partial Fulfillment

of the Requirements for the Degree

Master of Science

by

Joseph C. Chung

May 2008

UMI Number: 1458123

INFORMATION TO USERS

The quality of this reproduction is dependent upon the quality of the copy submitted. Broken or indistinct print, colored or poor quality illustrations and photographs, print bleed-through, substandard margins, and improper alignment can adversely affect reproduction.

In the unlikely event that the author did not send a complete manuscript and there are missing pages, these will be noted. Also, if unauthorized copyright material had to be removed, a note will indicate the deletion.

UMI[®]

UMI Microform 1458123

Copyright 2008 by ProQuest LLC.

All rights reserved. This microform edition is protected against unauthorized copying under Title 17, United States Code.

ProQuest LLC
789 E. Eisenhower Parkway
PO Box 1346
Ann Arbor, MI 48106-1346

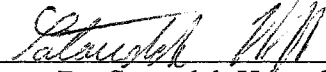
© 2008

Joseph C. Chung

ALL RIGHTS RESERVED

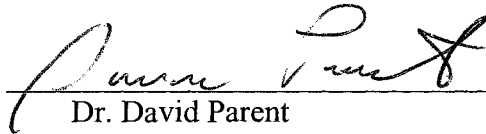
APPROVED FOR THE DEPARTMENT OF ELECTRICAL ENGINEERING

Advisor



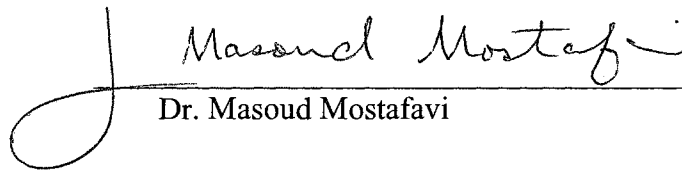
Dr. Sotoudeh Hamed-Hagh

Co-Advisor



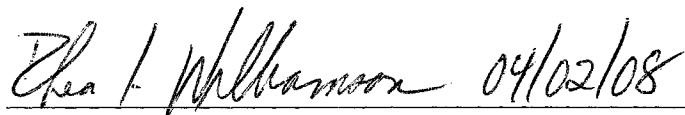
Dr. David Parent

Co-Advisor



Dr. Masoud Mostafavi

APPROVED FOR THE UNIVERSITY



ABSTRACT

DESIGN FLOW APPROACH FROM INDUCTORS TO ANTENNA AT PCB LEVEL

by Joseph C. Chung

Integrated circuits, ICs, and printed circuit boards, PCBs, need to be designed optimally to complement each other for system level functionality. This is critical in radio frequencies where inductors and antennas are essential to the system. For inductor design, PCB is better over silicon as it delivers higher inductance and quality factor for given cost/area. PCB also provides the ability to design high gain antennas. This thesis proposes a design flow from inductors to antennas for students in system design. The flow includes theory, design, simulations as well as fabrication and measurements. The goal is to characterize a PCB substrate through two inductors to optimize simulators for a GPS L1 antenna design. For intermediate frequency applications, the larger inductor at 200MHz has measured inductance of 95nH, resistance of 2.9Ω , and quality factor of 51. The antenna has a measured bandwidth of 250MHz and a return loss of $|-36|$ dB at 1.5754GHz.

ACKNOWLEDGEMENT

I would like to thank my M.S.E.E. thesis advisor, Dr. Sotoudeh Hamedi-Hagh, for his exceptional guidance. Also, I am grateful for his RFIC lab at San Jose State University where the measurements for this thesis were made possible.

I would like to thank Dr. G.A. Rezvani from RFMD for his invaluable advice on calibration and measurement techniques.

Also, I would also like to thank Sonnet Software Inc. and Agilent for their generosity in allowing the use of their tools.

In addition, I would like to thank my co-advisors, Dr. David Parent and Dr. Masoud Mostafavi for their support.

Last but not least, I would like to thank my mother, Grace, brother, Raymond, and girlfriend of eight years, Julie, for their patience and their understanding of the importance of my work in the completion of this thesis.

TABLE OF CONTENTS

1	INTRODUCTION	1
1.1	Inductor Background	1
1.2	Antenna Background	4
1.2.1	Antenna Applications - GPS Background	6
1.3	Summary and Thesis Outline.....	7
2	THEORY, ANALYSIS, AND DESIGN	9
2.1	Inductor	9
2.1.1	Inductance	9
2.1.2	Resistance	16
2.1.3	Quality Factor	19
2.2	Antenna	20
2.2.1	Proposed Geometry	21
2.2.2	Radiation Pattern.....	22
2.2.3	Directivity and Gain.....	24
2.2.4	Polarization	25
2.2.5	Impedance Bandwidth and Q-factor	29
2.3	Chapter Summary	33
3	SIMULATIONS	34
3.1	Inductors	34
3.1.1	Inductance	40
3.1.2	Resistance	41
3.1.3	Quality Factor	43
3.2	Transition from Inductor to Antenna	44
3.3	Antenna	46
3.3.1	Radiation Pattern.....	46
3.3.2	Directivity and Gain.....	47
3.3.3	Polarization	49
3.3.4	Impedance Bandwidth	50
3.4	Chapter Summary	51
4	MEASUREMENTS.....	52
4.1	Measurement Conditions	52
4.2	Calibration and De-embedding	53
4.2.1	VNA and Calibration	53
4.2.2	PCB Trace De-embedding	55
4.3	Inductors	59
4.3.1	Inductance	62
4.3.2	Resistance	64
4.3.3	Quality Factor	66
4.3.4	Results.....	67
4.4	Transition from Inductor to Antenna	68
4.5	Antenna	68
4.5.1	Impedance Matching.....	69

4.5.2	Results.....	70
4.6	Chapter Summary	71
5	CONCLUSION.....	72
	References.....	74

LIST OF TABLES

Table 1-1 Inductor Tradeoffs – PCB vs. Silicon.....	3
Table 1-2 Antenna Tradeoffs – PCB vs. Silicon.....	5
Table 3-1 ADS Antenna Dialog.....	48
Table 4-1 Twelve Error Terms	54
Table 4-2 Inductor ‘A’ Parameter Summary	67
Table 4-3 Inductor ‘B’ Parameter Summary	68
Table 4-4 Summary of Impedance Matching and Bandwidth	70

LIST OF FIGURES

Fig. 1-1 Typical Toroid.....	1
Fig. 1-2 Typical Rod.....	2
Fig. 1-3 Model for Inductor on Silicon.....	3
Fig. 1-4 Model for Inductor on FR4 PCB.....	3
Fig. 1-5 Typical Yagi Antenna.....	4
Fig. 1-6 Typical Whip Antenna.....	5
Fig. 2-1 Visual of Current Flow Direction for Square Inductor.....	12
Fig. 2-2 Dimensions of Proposed Square Inductor 'A'.....	15
Fig. 2-3 Dimensions of Proposed Square Inductor 'B'.....	16
Fig. 2-4 Proposed Geometry of Antenna.....	22
Fig. 2-5 Polar References.....	23
Fig. 2-6 Visual of Linear Polarization.....	26
Fig. 2-7 Visual of (a) Right Hand Circular Polarization and (b) Left Hand Circular Polarization.....	27
Fig. 2-8 Various Circular Polarization Patch Methods.....	28
Fig. 3-1 ADS Layout of Inductor 'A'.....	34
Fig. 3-2 ADS Layout of Inductor 'B'.....	35
Fig. 3-3 Sonnet Layout of Inductor 'A'.....	36
Fig. 3-4 Sonnet Layout of Inductor 'B'.....	36
Fig. 3-5 Simulated S_{11} Parameters of (a) Inductor 'A' and (b) Inductor 'B'.....	37
Fig. 3-6 Simulated S_{21} Parameters of (a) Inductor 'A' and (b) Inductor 'B'.....	38
Fig. 3-7 Simulated S_{12} Parameters of (a) Inductor 'A' and (b) Inductor 'B'.....	39
Fig. 3-8 Simulated S_{22} Parameters of (a) Inductor 'A' and (b) Inductor 'B'.....	39
Fig. 3-9 Simulated Inductance of Inductor 'A'.....	40
Fig. 3-10 Simulated Inductance of Inductor 'B'.....	41
Fig. 3-11 Simulated Resistance of Inductor 'A'.....	42
Fig. 3-12 Simulated Resistance of Inductor 'B'.....	42
Fig. 3-13 Simulated Resistance of Inductor 'A'.....	43
Fig. 3-14 Simulated Resistance of Inductor 'B'.....	44
Fig. 3-15 Flow Chart of Design Process.....	45
Fig. 3-16 E-field Radiation Pattern.....	47
Fig. 3-17 Sonnet Theta vs. Gain.....	48
Fig. 3-18 Right Hand Circular Polarization Pattern.....	49
Fig. 3-19 Simulated S_{11} of Antenna Design.....	50
Fig. 4-1 Transfer Data from Network Analyzer to Matlab.....	52
Fig. 4-2 Fabricated Inductors with De-embedding Circuits.....	56
Fig. 4-3 Example of the Effects of Trace De-embedding (Using Open-Shorts).....	57
Fig. 4-4 Layout for Fabrication for Inductor 'A'.....	59
Fig. 4-5 Layout for Fabrication for Inductor 'B'.....	59
Fig. 4-6 Measured S_{11} Parameters of (a) Inductor 'A' and (b) Inductor 'B'.....	60
Fig. 4-7 Measured S_{12} Parameters of (a) Inductor 'A' and (b) Inductor 'B'.....	61
Fig. 4-8 Measured S_{21} Parameters of (a) Inductor 'A' and (b) Inductor 'B'.....	61

Fig. 4-9 Measured S_{22} Parameters of (a) Inductor 'A' and (b) Inductor 'B'	62
Fig. 4-10 Measured Inductance of Inductor 'A' Relative to Simulations.....	63
Fig. 4-11 Measured Inductance of Inductor 'B' Relative to Simulations.....	64
Fig. 4-12 Measured Resistance of Inductor 'A' Relative to Simulations	65
Fig. 4-13 Measured Resistance of Inductor 'B' Relative to Simulations	65
Fig. 4-14 Measured Q-factor of Inductor 'A' Relative to Simulations.....	66
Fig. 4-15 Measured Q-factor of Inductor 'B' Relative to Simulations.....	67
Fig. 4-16 Front and Back Pictures of L-ground Plane with Lowercase-h Configuration and Cornered Patch	69
Fig. 4-17 Measured S_{11} Parameter Relative to Simulations	70

1 INTRODUCTION

At the printed circuit board (PCB) level, components such as inductors and antennas are created from similar traces, yet their application purposes vary drastically. Inductors are passive components which optimally retains as much energy within the traces as possible. Antennas on the other hand, optimally radiate as much energy as possible. The inductor design flow will lead into the design of an antenna for global positioning system (GPS) applications. The general background as well as information specific to PCB vs. silicon will be discussed, followed by the thesis outline.

1.1 Inductor Background

Inductors are electronic components which oppose current changes and at the same time create magnetic fields [1]. Inductors are as essential to electronics as capacitors and resistors which are used in various electronics, especially for RF circuits and transformers [2]. Historically inductors come in various forms such as in a toroid as shown in Fig. 1-1 or in a rod form as shown in Fig. 1-2 [2].

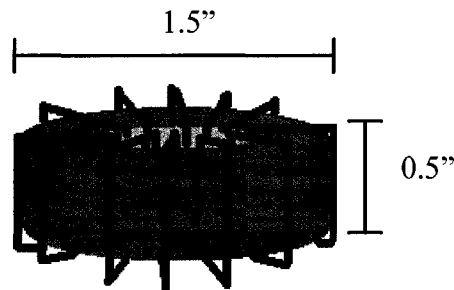


Fig. 1-1 Typical Toroid

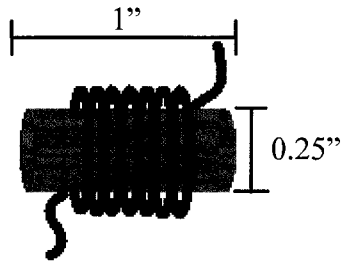


Fig. 1-2 Typical Rod

As one can see in Fig. 1-1 and Fig. 1-2, physically, the traditional inductors have been large and occupy a significant amount of space. Also, the mentioned types of inductors are three dimensional as opposed to two dimensional planar inductors.

Planar inductors may be created on silicon or on typical FR4 PCB. Analyses of tradeoffs between the two types of substrates are performed. First, the cost of the amount of area used to create an inductor in silicon by far exceeds the equivalent cost in PCB. Also, inductors designed in silicon require special steps and processes compared to inductors designed on PCB. For example, extra steps as creating trenches in silicon described in [3] or steps using suspension methods described in [4]-[5], show the complexity. The methodology to distinguish merits of inductors is through the Q-factor or quality factor described further in chapter 2 section 1.3, however, Q-factor on silicon is much lower than on PCB. The magnitude for inductors on silicon is typically between 10 and 20, usually much less than 25, similar to the range of the inductances with units in nH [3]-[6]. Inductors on PCB with FR4 substrate inherently have the capability of higher inductance and Q-factor in the standard process. This paper will show a PCB based inductor with at least twice the Q-factor of [3]-[6]. Table 1-1 summarizes the mentioned tradeoffs.

Table 1-1 Inductor Tradeoffs – PCB vs. Silicon

<i>Tradeoffs:</i>	Silicon Inductor	FR4 PCB Inductor
Area/Cost	High	Low
Fabrication Complexity	High	Low
Inductance	Low	High
Q-factor	Low	High

To further analyze the differences between creating inductors on silicon and FR4, representative models are analyzed. Fig. 1-3 [7] shows the model for inductors on silicon, while Fig. 1-4 [8] shows the model for the FR4 PCB inductor.

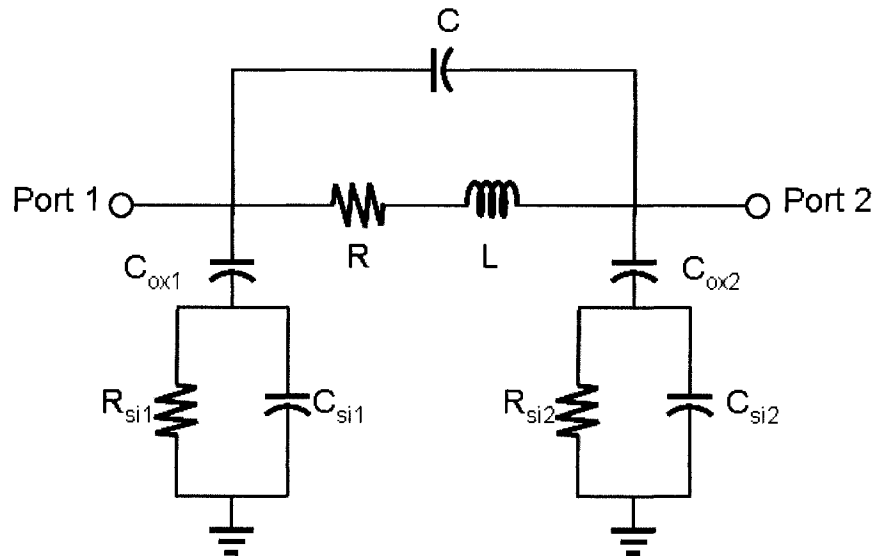


Fig. 1-3 Model for Inductor on Silicon

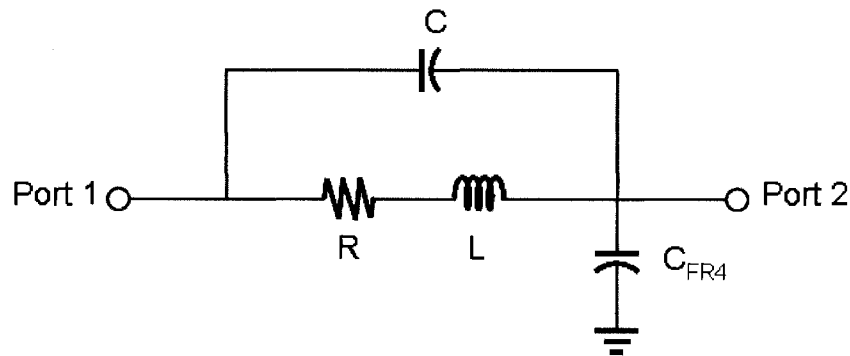


Fig. 1-4 Model for Inductor on FR4 PCB

The silicon inductor model shows the inherent inductance, L , and the inherent series resistance, R . The parasitic capacitance from the oxide between the metal and silicon is denoted as C_{ox} . Within the silicon, C_{si} and R_{si} are parasitic capacitance and resistance modeled in parallel to each other due to the substrate characteristics, affecting the Q-factor [9]. Both Fig. 1-3 and Fig. 1-4 show a coupling capacitor C between the two ports. Fig. 1-4 shows the actual inductance, L , and the series resistance, R , however, with only a single source of substrate parasitic, C_{FR4} . In comparing Fig. 1-3 and Fig. 1-4, it is evident that less parasitics are in PCB compared to silicon.

In analyzing the tradeoffs, the inductors are to be designed on FR4. The applications for the inductors would be for intermediate frequency purposes, which complements other necessary RF components such as the antenna for system level applications.

1.2 Antenna Background

Historically, antennas are geometrically large as in the case of the typical Yagi (Fig. 1-5) [10] and the typical whip (Fig. 1-6) [10].

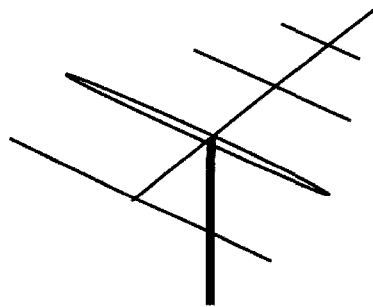


Fig. 1-5 Typical Yagi Antenna

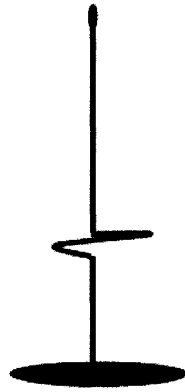


Fig. 1-6 Typical Whip Antenna

Again, as in the introduction to inductors, antennas may also be improved from three-dimensional to two dimensional by decreasing the size creating an efficient use of space. The two substrate options are PCB and silicon. As in the case of the inductors, the antenna fabrication is more complex and more expensive on silicon than PCB. Typically the dielectric of PCB is much less than on silicon substrates, which helps the radiation properties. The mentioned tradeoffs are shown in a summarized form in Table 1-2.

Table 1-2 Antenna Tradeoffs – PCB vs. Silicon

<i>Tradeoffs:</i>	Silicon Antenna	FR4 PCB Antenna
Area/Cost	High	Low
Fabrication Complexity	High	Low
Radiation Efficiency	Low	High
Dielectric Constant	High	Low

PCB microstrip traces, shown in Table 1-2, as a better option are actually very popular for antenna design. Although the concept of microstrip antennas was discovered in the early 1950s, improved fabrication techniques helped it gain popularity in the 1970s after advancement of photolithography technology [11]. Even today, PCB microstrip antennas are still becoming improved upon in terms of theory

and fabrication process. As a result, microstrips antennas on PCB are chosen to be used on many portable devices for various applications.

1.2.1 Antenna Applications - GPS Background

The GPS market has grown substantially in the recent years. Due to the cost effectiveness and portability, handheld GPS devices are popular. The idea of GPS was invented by Ivan Getting and Bradford Parkinson during the 1950s; it is described as a system of moving satellites that enables the determination of physical position relative to time difference of the transmitted signals [12]. In 1969, the U.S. Defense Department started its own research and eventually created 24 satellites, launching them in 1978, which were operational by 1995, having capability of down to 10 meter accuracy [13]. Although the GPS system was originally intended for military use, due to a 1983 airline incident, President Ronald Reagan promised its availability to civilians after its completion to promote public safety [13]. For that reason, the general public is able to use portable GPS devices today.

An important aspect of the handheld GPS device is the antenna that ensures a strong signal. GPS satellites send their signals on to the L1 band with a carrier frequency of 1575.42MHz and a bandwidth of 2.046MHz with RCHP, right hand circular polarization [14]. The antenna portion of this paper will focus on the design of a GPS application specific antenna. The proposed antenna differs from typical GPS antennas in papers such as [15]-[17] by having a more relatively directive radiation pattern with maximum intensity in the PCB forward direction with a theta in

70° range for mounting purposes. The presented antenna design is a “L-ground plane with lowercase-h configuration and cornered patch.”

1.3 Summary and Thesis Outline

The goal of the project is to create a design flow from characterizing a two port inductor, fully characterizing the PCB board, and then designing an antenna from the optimized simulators. This thesis is categorized into five chapters. The first chapter is the introduction, which describes the brief background of inductors and antennas. Chapter 2 explains the analysis and design of the inductors and the antenna. Chapter 3 discusses the simulations that were performed for the inductors and the antenna. Chapter 4 shows the measurements both the inductors and antenna. Finally, chapter 5 is the conclusion, which wraps up the entire project. An important point is that the design, simulation, and measurement for the inductor were fully completed before the antenna’s design, simulation, and measurement were performed; however, for clear organization of the ideas, the three topics are explained in parallel.

The result of this thesis is to create a pair of inductors with values of 55nH at around 300MHz and 100nH at 200MHz for intermediate frequency applications. The first inductor, which will be denoted as inductor ‘A’ is an initial trial having a smaller Q-factor goal in the range of 30, while inductor ‘B’ has a much higher Q-factor of at least 50. Both inductors are to have a reasonable 3.5 turns. The completed inductors will allow optimization of the simulators through the characterization of the PCB to

enable the design of an antenna centered at 1575.42MHz with a bandwidth much greater than 2.046MHz and is right hand circularly polarized.

2 THEORY, ANALYSIS, AND DESIGN

This chapter will present the theory, analysis, and design of a pair of inductors as well as an antenna. The inductor section will describe inductance, resistance, and quality factor parameters. Following, the antenna section will describe the proposed geometry, radiation pattern, directivity and gain, polarization, as well as impedance bandwidth and Q-factor.

2.1 Inductor

The objective of the inductor design is to provide characteristics of a two port component to better understand the PCB characteristics, which may also be used for intermediate applications. Parameters such as inductance, resistance, and Q-factor are computed and analyzed in the following sections. The goal is to create a 55nH inductor at 300MHz with a Q-factor of around 30 and a 100nH inductor at 200MHz with at least a Q-factor of 50. Both inductors shall be designed with reasonable 3.5 turns. The general inductor theory regarding the inductance, resistance, and quality factor will be presented followed with followed with specific PCB calculations.

2.1.1 Inductance

Inductors innately consist of two types of inductances: self-inductance and mutual inductance. Both self-inductances and mutual-inductances are described in the units of Henry. A Henry has units of Weber per Ampere, which is essentially magnetic flux in relation to current [1]. Traditionally inductance is created through

coils, which is how the general definitions of mutual and self inductance will be explained.

Mutual inductance is generated when a magnetic field is created from the changing current of one coil which creates flux through a second adjacent coil defined by [18]

$$L_{12} = \frac{N_2 \Phi_{12}}{I_1} \quad (2.1)$$

and vice versa,

$$L_{21} = \frac{N_1 \Phi_{21}}{I_2} \quad (2.2)$$

The terms in the shown equations (2.1) and (2.2) are the number of turns in a coil, N , the magnetic flux, Φ , and the current, I . The characteristics may be seen from the circuit point of view where voltage is important, therefore, the induced voltage of the two coil circuits are shown as [19]

$$v_2 = L_{12} \frac{di_1}{dt} \quad (2.3)$$

and

$$v_1 = L_{21} \frac{di_2}{dt} \quad (2.4)$$

As the instantaneous current changes in one coil, a voltage in the second coil is induced through the flux that links the two coil circuits. From analysis, mutual inductance can be seen as a phenomenon which determines the magnitude of voltage relative to the change in current with respect to time.

Self inductance is generated when a magnetic field is created from current within a coil as opposed to (2.1) and (2.2), because the flux and current are within one coil [18]. Self induction occurs in a coil itself and innately generates a voltage through the flux created in an electromotive force ϵ that is in the opposite direction, where $\epsilon = -L(dI/dt)$ [18]-[19].

These mentioned theories are for generalized cases; however, inductors can also be analyzed for implementation on PCB.

Inductors on PCB are planar parallel to the surface of the PCB. The inductances of PCB inductors depend specifically on the geometry. The total inductance is determined by the mutual inductance and self inductance.

In the mentioned general inductance theory, mutual inductance was described with two separate inductors; however, mutual inductance may also occur amongst embedded parallel conductive traces within a single inductor, particularly on PCB [8]. The equations (2.1) and (2.2) can be utilized in terms of two segments within an inductor instead of two separate inductors. In a planar PCB inductor, to calculate the mutual inductance, the whole inductor needs to be broken up into segments and analyzed with respect to the corresponding coupling parallel traces. The mutual inductance may be positive or negative depending on the direction of the currents on the parallel segments of the PCB inductor mention in [8] and [20], where the concept is shown in the Fig. 2-1.

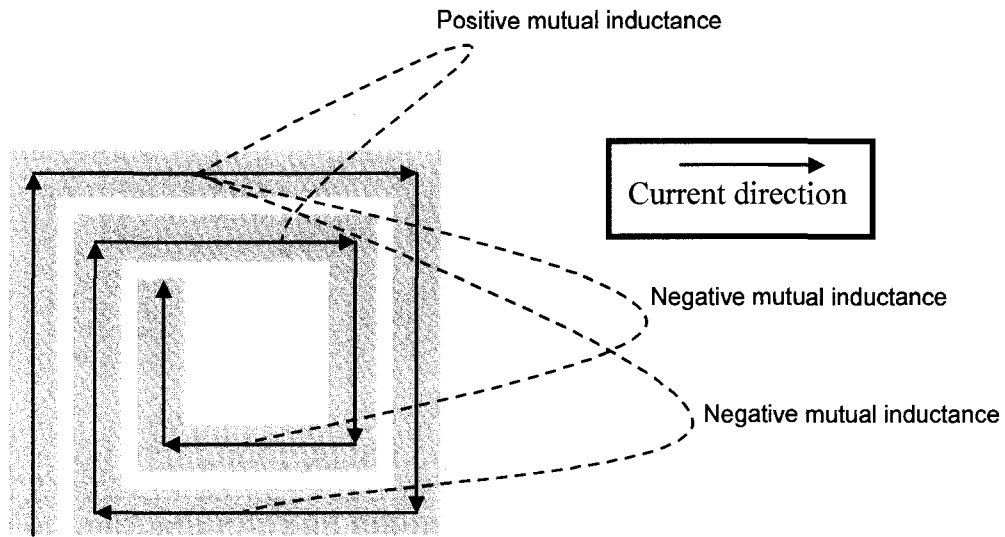


Fig. 2-1 Visual of Current Flow Direction for Square Inductor

Two methods of relating the geometries of the inductors to inductance values on PCB will be discussed. A more detailed and complex theoretical method will first be discussed, which determines the total inductance after the mutual and self inductance are analyzed. The second method directly relates the total inductance to the geometry.

The first method is to determine the mutual inductance by using an equation considering l for the length of the a trace, d for the distance between the two traces, and w for the width of the traces, with units in centimeters for [20]

$$L_{Mutual} = 2l \left[\ln\left(\frac{l}{G}\right) + \left(1 + \left(\frac{l^2}{G^2}\right)\right)^{\frac{1}{2}} \right] - \left(1 + \frac{G^2}{l^2}\right)^{\frac{1}{2}} + \left(\frac{G}{l}\right), \quad (2.5)$$

where G is [20]

$$G = e^{\left(\ln d - \left(\frac{1}{12 \left(\frac{d}{w} \right)^2} + \frac{1}{60 \left(\frac{d}{w} \right)^4} + \frac{1}{168 \left(\frac{d}{w} \right)^6} + \frac{1}{360 \left(\frac{d}{w} \right)^8} + \frac{1}{660 \left(\frac{d}{w} \right)^{10}} + \dots \right) \right)} \quad (2.6)$$

The polarity of L_{Mutual} , mutual inductance, depends on the relative current direction as mentioned earlier in Fig 2-1.

To determine the self inductance of the particular mentioned planar inductor, the conductive trace may be analyzed through [8]

$$L_{self} = 0.002l \left[\ln \left(\frac{2l}{0.2232(w+h)} \right) - 1.25 + \frac{(w+h)}{3l} + \left(\frac{\mu}{4} \right) T \right]. \quad (2.7)$$

The term μ relates to the permeability and h is the height of the PCB substrate. Again, w is the width of the conductive trace in centimeters, and as [8] mentions, T , is a term dependent on the thickness of the trace and frequency, that can be approximated to be 1 for most cases [20].

Finally, the total inductance for the inductor is determined by summing all the mutual inductances and self inductances segments in [8]

$$L_{Total} = \Sigma L_{self} - \Sigma |L_{Mutual}^-| + \Sigma L_{Mutual}^+ \quad (2.8)$$

As one may see, the first mentioned process of determining the geometry from desired inductance, or vice versa, is very complicated and tedious. Therefore, the following method is much more practical and combines the mutual and self inductance into a single formula.

For design calculations of square planar inductors before beginning

simulations, the method discussed [21] is sufficient. The method calculates the inductance in nanohenries through the equation [21]

$$L_{square} \cong 8.5DN^{\frac{5}{3}}, \quad (2.9)$$

where D is the distance between the outer edges of the square inductor, in centimeters, and N is the number of turns within the inductor.

As mentioned earlier, two inductors designs with various values and trace thickness will be created to have a broader view of the PCB characteristics. First a 55nH inductor denoted as ‘A’ will be designed followed by a 100nH inductor denoted as ‘B.’

The distance between the outer edges of the square for inductor ‘A,’ D_A , is determined by first choosing the number of turns, N, to be 3 ½ and setting $L_{square}=55\text{nH}$. The calculation follows as:

$$D_A \approx \frac{55}{8.5(3.5)^{\frac{5}{3}}} \approx .8019\text{cm}$$

Since the typical units used for PCB design are in mil, which is 1/1000 on an inch, converted, D_A is 315.7 mil. In the actual layout to fit the traces, D_A is set to 310 mil to accommodate the grid. Due to the fact that (2.9) only specifies the overall square dimension and the number of turns, the width of the conductor traces are chosen for reasonable fit within the dimension limitations. Since flexibility is allowed for the trace width, w, and spacing between the traces, s, reasonable values of $w = 30$ mil and $s = 10$ mil are set, as shown in Fig. 2-2.

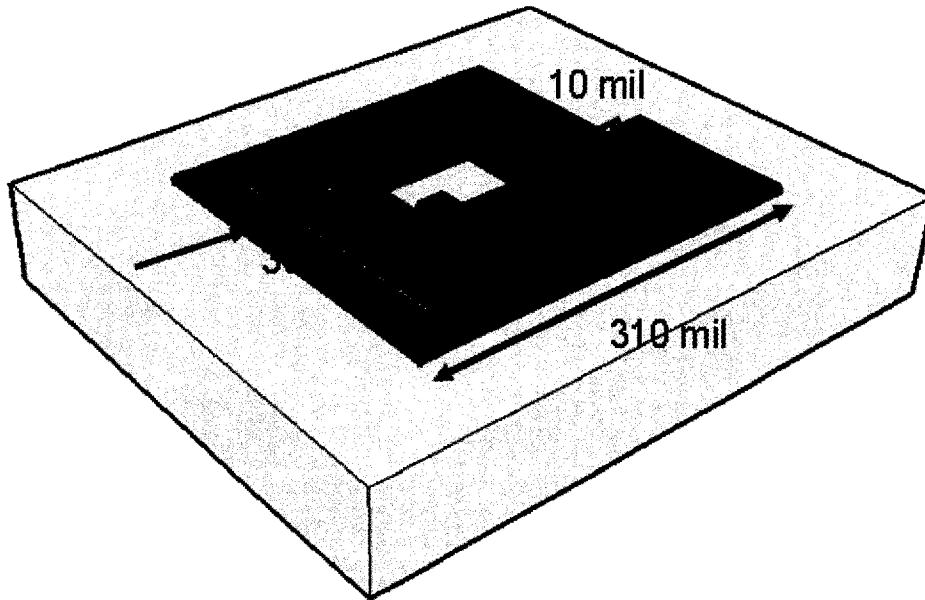


Fig. 2-2 Dimensions of Proposed Square Inductor ‘A’

Inductor ‘B’ will also be designed with $3\frac{1}{2}$ turns for N but with $L_{square}=100\text{nH}$. The distance between the outer square inductor ‘B,’ D_B , is calculated as follows:

$$D_B \approx \frac{L_{square}}{8.5N^3} \cong \frac{100}{8.5(3.5)^3} \cong 1.458\text{cm}$$

Therefore, converted to mil, D_B is 574.01 mil. After the dimension is rounded to a grid, the distance between the rectangular edges becomes $D_B=570$ mil as shown in Fig. 2-3.

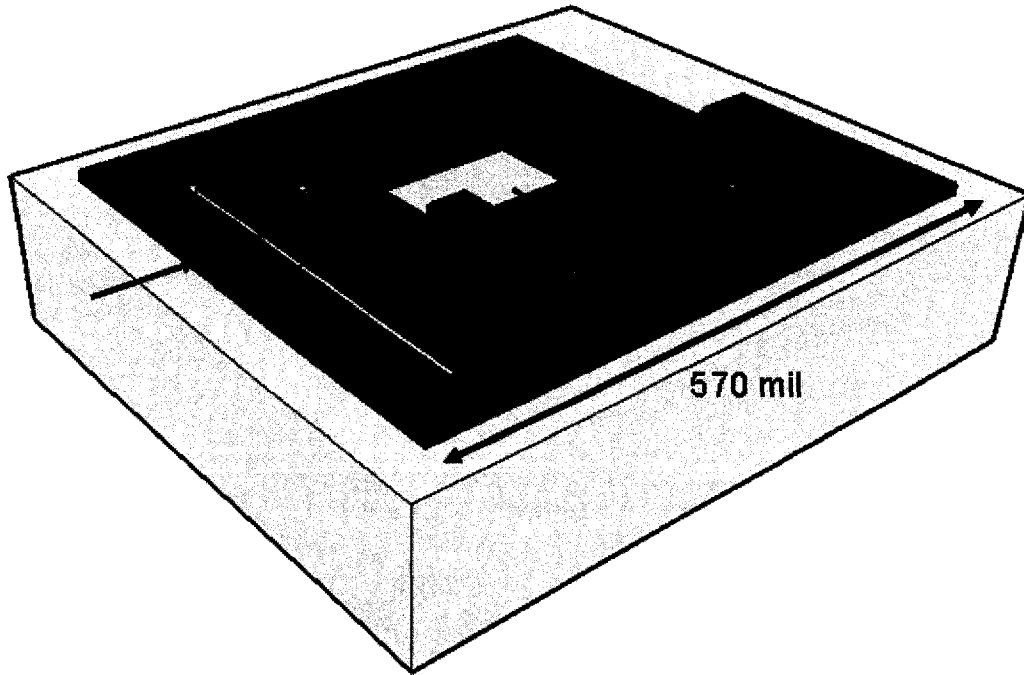


Fig. 2-3 Dimensions of Proposed Square Inductor ‘B’

Again, flexibility is given for the width and space for the traces. For the design inductor ‘B’, the width of 60 mils with even spacing of 10 mils between the traces works to maintain $D_B=570\text{mil}$.

2.1.2 Resistance

In terms of physics and electronics, resistance is the difference in potential relative to the current as shown in ohm’s law, $R=\Delta V/I$ for conductive materials [18].

Resistance can also be defined with [1],

$$R = \frac{l}{\sigma A}, \quad (2.10)$$

where l is the length of the conductor, A is the cross sectional area, and σ is the conductivity with units of $1/(\Omega \cdot \text{m})$. An ideal conductor is lossless if their

conductivity is infinitely high, however, in the real-world, conductors have losses due to the finite conductivity.

Although the resistance at operating frequency is the interest for the inductors, the DC resistance values are determined as a reference for comparison. The general resistance theory is interpreted in practical equations in relation to PCB design, for both DC and high frequencies, which will explained along with calculations.

Microstrip resistance is an important characteristic of a PCB inductor, which changes depending on the frequency the measurements are analyzed at, either DC or at a high frequency. At DC, derived from the (2.10), the equivalent resistance of PCB a microstrip trace defined by [22]

$$R_{DC} = \frac{l}{\sigma wt}, \quad (2.11)$$

where w , t , l , and σ are the width, thickness, length, and conductivity of the conductor, respectively.

The order of calculations for the DC resistance is first performed for the 55nH inductor then for the 100nH inductor. As seen in the DC resistance equation in (2.11), the conductivity is needed for calculations. After analysis and experimentation, the determined conductivity value used is 1.36×10^6 S/m, which is further explained in chapter 3 section 2.

The DC resistance for the 55nH inductor 'B' with 30 mil trace width converted to 7.62×10^{-4} m, and trace thickness of 1.4 mil converted to 3.556×10^{-5} m, are calculated as follows:

$$R_{DC A} = \frac{80 \times 10^{-3}}{(1.36 \times 10^6)(7.62 \times 10^{-4})(3.56 \times 10^{-5})} = 2.17 \Omega$$

The DC resistance for the 100nH inductor 'B' with the 60 mil trace width converted to 1.52×10^{-3} m, and trace thickness of 1.4 mil converted to 3.56×10^{-5} m is calculated as

$$R_{DC B} = \frac{150 \times 10^{-3}}{(1.36 \times 10^6)(1.52 \times 10^{-3})(3.56 \times 10^{-5})} = 2.12 \Omega .$$

The respective DC resistances for inductor 'A' and 'B', being 2.17Ω and 2.12Ω intuitively make sense because inductor 'B' has wider traces, which is in agreement with (2.10).

Importantly, the resistances are determined at the specific operating frequencies. As frequency increases, particular to higher values, the resistance changes because charges will swarm towards a relatively smaller area at the outer edge of the conductor against the dielectric, with a phenomenon known as the skin depth, which is defined as [23]

$$\delta = \sqrt{\frac{2}{\omega \mu \sigma}} . \quad (2.12)$$

Since at high frequencies only the skin depth portion of the conductor is conductive, intuitively the thickness term is replaced in (2.11) with the frequency dependent term to determine resistance in

$$R_{HF} = \frac{l}{\sigma w \delta} . \quad (2.13)$$

First, the resistance at operating frequency will be determined for inductor 'A'

at 300MHz to be:

$$R_{HFA} = \frac{80 \times 10^{-3}}{(1.36 \times 10^6)(7.62 \times 10^{-4}) \left(\sqrt{\frac{2}{2\pi(3 \times 10^8)(4\pi \times 10^{-7})(1.36 \times 10^6)}} \right)} = 3.1\Omega$$

From inspection, R_{DCA} with a value of 2.12 Ω is raised to 3.1 Ω for RF_{HFA} at 300MHz, which confirms the changes of resistance within the inductor, is due to the higher frequency. Again, the purpose of the designed inductors would be in applications for intermediate frequencies, therefore, a variety of frequencies may be used.

Inductor 'B' will is designed to operate in the 200MHz range, therefore using (2.13), the high frequency resistance can be calculated as

$$R_{HFB} = \frac{150 \times 10^{-3}}{(1.36 \times 10^6)(1.52 \times 10^{-3}) \left(\sqrt{\frac{2}{2\pi(2 \times 10^8)(4\pi \times 10^{-7})(1.36 \times 10^6)}} \right)} = 2.38\Omega$$

As can be seen, the R_{HFB} shows an increase over R_{DCB} , which confirms the frequency dependency and intuition.

2.1.3 Quality Factor

In order to distinguish various inductors, the effectiveness of an inductor should be qualitatively quantified. The quality factor or Q-factor is a measurement which compares the amount of energy stored, W_{stored} , in an inductor to the amount of energy dissipated, $W_{\text{dissipated}}$, in an inductor every cycle as shown in the following [23]:

$$Q = \frac{W_{stored}}{W_{dissipated}} (\text{frequency_dependency}) . \quad (2.14).$$

In terms of the components, the quality factor may also be represented in terms of the resistance, R, and inductance, L, by [21]

$$Q = \frac{\omega L}{R} \quad (2.15)$$

where the frequency dependency can be seen. However, the Q-factor is typically evaluated at a frequency is far below resonant [24]. The Q-factors for the two inductors are determined. The Q-factor of an inductor ‘A’ with an inductance of 55nH and a resistance of 3.1 Ω at a frequency of 300MHz is computed as follows:

$$Q_A = \frac{2\pi(300 \times 10^6)(55 \times 10^{-9})}{3.10} = 33.4 .$$

The quality factor for the inductor ‘B’ 200MHz design with the corresponding calculated resistance of 2.38 Ω and 100nH inductor parameter is computed as follows:

$$Q_B = \frac{2\pi(200 \times 10^6)(100 \times 10^{-9})}{2.38} = 52.8 .$$

The quality factor for inductor ‘B’ is 53, which is reasonably high.

2.2 Antenna

The proposed antenna project is a GPS patch. A brief overview of GPS technology follows.

Technically, GPS has two services, the Precise Positioning Service for the

military and the Standard Positioning Service, SPS, which is less accurate, but still very effective for civilians [14]. SPS transmits messages on to the L1 signal at the carrier frequency 1575.42MHz with a bandwidth of 2.046MHz with right hand circular polarization [14]. This project will focus on the L1 civilian frequency.

The subsections for the antennas design will include the proposed geometry, a brief description of radiation pattern, directivity compared to gain, polarization, and impedance bandwidth compared to Q-factor.

2.2.1 Proposed Geometry

A starting point to design a reasonable small antenna is the classic inverted-f [25]-[26], known for its compactness. After analyzing the parameters such as polarization and radiation patterns, a modified antenna is design is proposed. The proposed unique antenna, “L-ground plane with lowercase-h configuration and cornered patch,” is shown in Fig. 2-4.

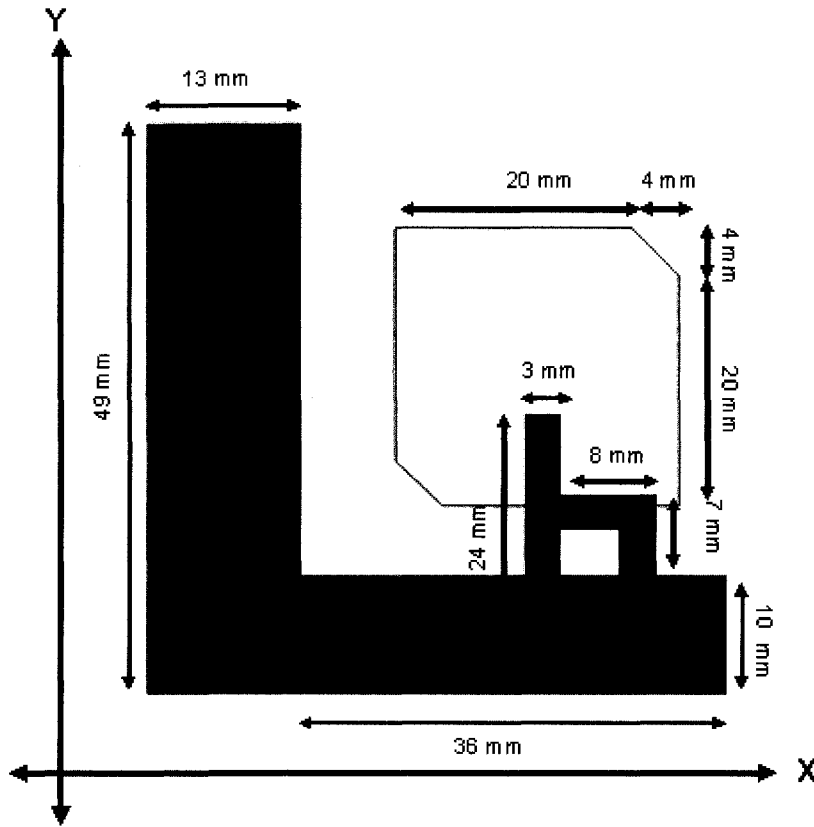


Fig. 2-4 Proposed Geometry of Antenna

The following subsections describing the parameters will all explain theories as well their influences towards the design of the proposed antenna.

2.2.2 Radiation Pattern

In terms of physics, radiation occurs when electrons move from a time respective varying voltage or current and causes acceleration creating a magnetic and a Coulomb field [27]. In particular, the radial electric field created is [27]

$$E_r = \frac{-q}{4\pi\epsilon_0 r^2}, \quad (2.16)$$

where q is the electron charge in Coulombs, r is the distance, and ϵ_0 is the permittivity

of free space. The fields influence the radiation patterns, which will be explained in detail.

Radiation patterns define an antenna's electric field characteristics. It is important to determine the unique far-field characteristics of an antenna. One method to determine the radiation pattern is based on the electric surface current model, which for rectangular patches would be [11]

$$E_{\phi}(\theta, \phi) = \sin \phi \left(\frac{j\omega\mu_0}{4\pi \cdot r} \right) e^{-jk_0 r} (CurrentChar)(GndEff) \quad (2.17)$$

$$E_{\theta}(\theta, \phi) = -\cos \phi \left(\frac{j\omega\mu_0}{4\pi \cdot r} \right) e^{-jk_0 r} (CurrentChar)(GndEff) \quad (2.18)$$

The standard polar coordinates are used with phi and theta as shown in Fig. 2-5.

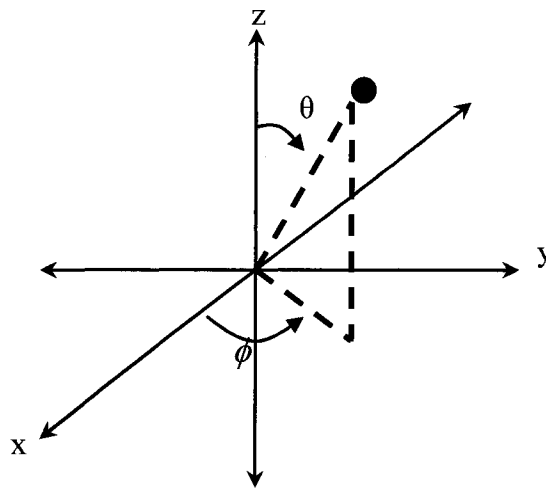


Fig. 2-5 Polar References

In equation (2.17) and (2.18), the radiation pattern can be observed to be highly dependent on distance, r , along with the permeability free space, μ_0 , and the wave number, k . The “*CurrentChar*” is the current characteristic term and “*GndEff*” is the

ground effects term. Both mentioned terms are related to the polar coordinates and are highly dependent on the antenna's geometry.

In terms of the proposed design, the left vertical side of the “L” shaped ground plane along the Y axis in Fig. 2-4 acts as a unique reflector to create a strong front beam in the +X direction, which dictates a particular desired radiation pattern.

The theory of the far-field radiation patterns can be found by finding the limit of the electric or magnetic field to infinity, such as [28]

$$\vec{E}(r \rightarrow \infty, \theta, \phi) = \vec{E}_{farfield}(\theta, \phi) \frac{e^{-jkr}}{r} \quad (2.19)$$

and

$$\vec{H}(r \rightarrow \infty, \theta, \phi) = \vec{H}_{farfield}(\theta, \phi) \frac{e^{-jkr}}{r}, \quad (2.20)$$

where the distance, r, can be seen to have a large influence with the electric and magnetic fields.

2.2.3 Directivity and Gain

Directivity and Gain are related to maximum radiation density. Directivity is the concentration of radiation intensity relative to the average radiated power, described in polar coordinates in [28]

$$D(\theta, \phi) = \frac{4\pi \left(\max \left(\frac{1}{2} (E_{farfield}(\theta, \phi) \times H_{farfield}^*(\theta, \phi)) \right) \right)}{\frac{1}{2} \int_{\Omega} E_{farfield} \times H_{farfield}^* \cdot d\Omega}. \quad (2.21)$$

Essentially, the denominator is the average radiated power through the Poynting

vector [29], in Watts, which is similar to determining the gain [28] in

$$G(\theta, \phi) = \frac{4\pi \left(\max \left(\frac{1}{2} (E_{farfield}(\theta, \phi) \times H_{farfield}^*(\theta, \phi)) \right) \right)}{P_{input}}. \quad (2.22)$$

The gain relates the maximum intensity to the input power instead. The variation between the gain compared to the directivity is due to the loss, which the efficiency, e , may be determined in [28]

$$e = \frac{G(\theta, \phi)}{D(\theta, \phi)}. \quad (2.23)$$

The efficiency is essentially the ratio of the gain to the directivity.

The directivity desired for the proposed specific design is to have the main beam at $\phi = 0^\circ$, which is achieved by the reflector reflecting the fields in the opposite 180° direction, creating the intense forward zero degrees ϕ power.

2.2.4 Polarization

Antennas also can be characterized by a polarization behavior. Polarization is a characteristic of the EM waves in regards to the varying vector positions with respect to time [29]. A linear polarization implies that the waves move in a straight line when seen in a two dimensional view. Therefore a linear electrical field vector moving along the x-axis and propagating respect to time on the z-axis may be shown as [29]

$$\vec{E} = \vec{a}_x E_o^+ e^{-jkz}, \quad (2.24)$$

where k is the wavenumber that is dependent on the wavelength defined as $k=2\pi/\lambda$.

As one may see, the equation (2.24) shows that although the wave is moving forward along the z-axis, the magnitude of the electric field is changing (increasing and decreasing) linearly with respect to the x-axis. From a side view, the linearity may be seen in Fig. 2-6.

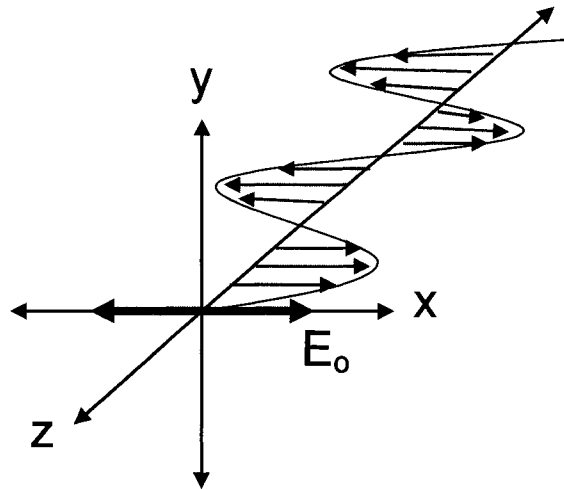


Fig. 2-6 Visual of Linear Polarization

From the electric field, the magnetic field may be correspondingly determined with [23].

$$\vec{H} = \frac{k}{\omega\mu} \vec{n} \times \vec{E}_0 \quad (2.25)$$

A type of non-linear polarization is circular polarization in which the \vec{E} field changes with respect to two axes. For example a sinusoidal waveform twists in circles amongst the x-y plane while traveling through the z axis. The a particular polarization waveform may be illustrated in the following equations [29]

$$\vec{E} = E_{10} \vec{a}_x e^{-jkz} - jE_{20} \vec{a}_y e^{-jkz} \quad (2.26)$$

or

$$\vec{E} = E_{10}\vec{a}_x e^{-jkz} + jE_{20}\vec{a}_y e^{-jkz} \quad (2.27)$$

which (2.26) is right-hand circularly polarized and (2.27) is left hand circularly polarized as long as E_{10} is equal to E_{20} . To understand how the equation shows the circular polarization, one may see that the electric field has x-vector and y-vector contributions in which the imaginary 'j' shows where the electric field is 90° phase in time. Equation (2.26) shows right hand circular polarization because the negative in front of 'j' indicates that 90° in time previously, the electric field was along the y-axis with the magnitude E_{20} and currently the electric field vector is along the x-axis with the magnitude E_{10} . An illustration for the right hand circular polarization is shown in the following Fig. 2-7 (a). Fig. 2-7 (b) represents equation (2.27) on the left hand shows circular polarization starting with E_{10} being aligned on the x axis and 90° later in time, the magnitude E_{20} becomes aligned on along the y axis [23].

Right Hand Circular Polarization

Left Hand Circular Polarization

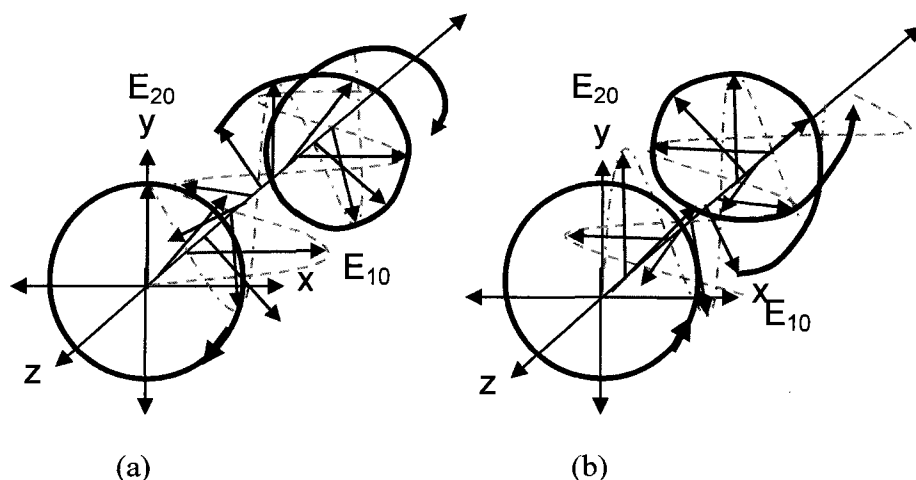


Fig. 2-7 Visual of (a) Right Hand Circular Polarization and (b) Left Hand Circular Polarization

A third type of polarization is an extension of circular polarization, which is

the elliptical polarization. This occurs when the magnitudes of the electric field, E_{10} and E_{20} , are not equal [29].

Particular to the proposed antenna, a linear electrical field vector moving up and down on the y -axis moving while propagating in the z -axis with respect to time is shown as [29]

$$\vec{E} = \vec{a}_y E_o^+ e^{-jkz}, \quad (2.28)$$

which is an innate characteristic of the “lower case-h” portion of the antenna without the cornered square patch in Fig. 2-4. Due to the modification of the antenna, the straight portion of the “h” became the $\lambda/8$ wavelength feed into the patch.

The GPS signals are sent with right hand circular polarization [14], as mentioned earlier. In order to provide a design with circular polarization, a few methods may be used such as having a dual feeds 90° out of phase fed into a patch, a single modified feed patch, a square patch with rectangular slot, or removing two opposite corners of a square patch as shown in Fig. 2-8 [30]-[31].

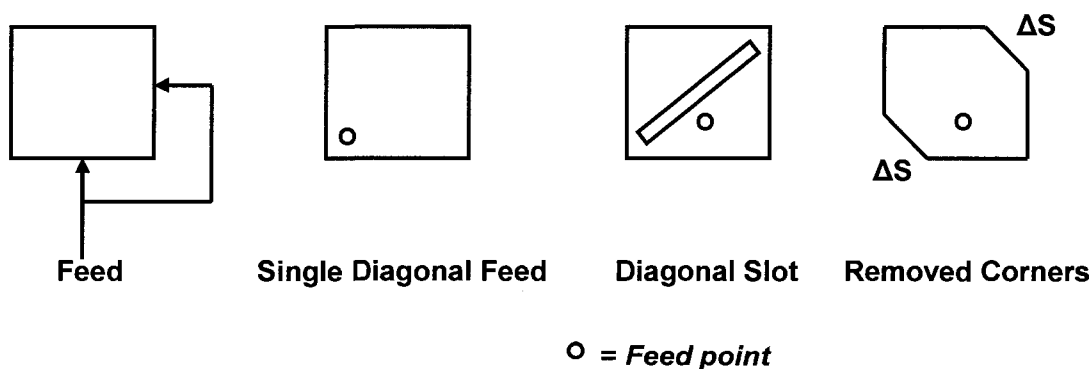


Fig. 2-8 Various Circular Polarization Patch Methods

As can be seen in Fig. 2-8 the last method on the right is used. The amount of

conductor removed, ΔS , from the total patch area, S , depends on the circular polarization due to the desired unloaded Q-factor in the equation [11]

$$\frac{\Delta S}{S} = \frac{1}{2Q_o}. \quad (2.29)$$

The Q-factor for antennas will be described in section 2.5.

The phenomenon of the circular polarization of the chosen patch is explained. Removing of the two corners of the square patch creates a 90° phase shift from the excited wave mode by creating a two ends with less capacitive corners distinguishing the waves from the more capacitive corners [30]. The mentioned right-hand circularly polarized is illustrated with the following equation [23]

$$\vec{E} = E_0 (\vec{a}_z - j\vec{a}_y) e^{-jkx} \quad (2.30)$$

because, again, the negative in front of 'j' indicates that 90° previously in phase time, the signal was aligned with the z-axis, which then becomes aligned to the y-axis. The order of the signal shows the clockwise movement in the right hand direction, while propagating in the +X direction.

2.2.5 Impedance Bandwidth and Q-factor

The bandwidth of an antenna is the frequencies in which the antenna is optimized to be used in. This section will show the tradeoff between impedance bandwidth and the quality factor.

The impedance seen into the antenna can have an imaginary part due to the capacitive or inductive nature and a real part which is pure resistance. The difference in the impedance creates a reflection of the signal and can be measured by [31]

$$\Gamma = \frac{Z_{in} - Z_0}{Z_{in} + Z_0}, \quad (2.31)$$

which Z_{in} is the input impedance and the Z_0 is the characteristic impedance. Ideally, the smaller the reflection coefficient, the better the power is transferred from one stage to the next. Also, optimal matching results in a smaller reflection coefficient.

From the reflection coefficient, the VSWR may be determined. The VSWR is the voltage standing-wave ratio (the relation between the maximum voltage to the minimum voltage) is a real number between one and infinite, which a 'one' value means a perfect match and that none of the signal is reflected [31]. The VSWR is an indication of how well components are matched, which may be determined from the reflection coefficient in the equation [22],

$$VSWR = \frac{1 + |\Gamma|}{1 - |\Gamma|}. \quad (2.32)$$

After determining the VSWR, the impedance bandwidth, which is the portion of the frequency spectrum that is expected to be well matched, may be determined in [32]

$$BW = \frac{VSWR - 1}{Q\sqrt{VSWR}}, \quad (2.33)$$

where Q is the quality factor of the antenna. In the analysis of equation (2.33), the bandwidth, BW , is inversely proportional to the quality factor, Q , which is a tradeoff. The quality factor is a measure of an antenna's physical limitation and performance which can be determined through [30]

$$Q = \frac{\omega W}{P}, \quad (2.34)$$

where W is the energy stored during resonance and P is the power loss.

In detail, other factors that affect the Q-factor are the radiator shape, the substrate thickness, the dielectric, and the losses of the conductors [11]. The Q-factor relation to the mentioned factors from [11] can be shown in a detailed Q-factor expression

$$Q_T = \frac{1}{\frac{1}{Q_c} + \frac{1}{Q_d} + \frac{1}{Q_R}}, \quad (2.35)$$

where the Q_d term is the contribution of the Q-factor through the dielectric materials of the PCB in [30]

$$Q_d = \frac{2 \cdot \pi \cdot \epsilon_r \cdot \epsilon_0 \cdot f}{\sigma_d}, \quad (2.36)$$

with the ϵ dielectric term, the f the frequency term, and σ_d the bulk conductivity term.

The Q_c is the Q-factor contribution through the conductor loss, where [30]

$$Q_c = h \sqrt{\mu_0 \cdot \pi \cdot f \cdot \sigma}. \quad (2.37)$$

The h in (2.37) is the height in mm, the μ_0 is the permeability of free-space, the σ is the conductivity of the conductor, while f frequency of interest. In general, the Q_R term refers to the radiation Q-factor as in (2.34). Essentially the contributions of the inverses of Q_c and Q_d are so small, unlike $Q=Q_R$, which is larger [11].

With the general theory of impedance bandwidth for the antenna discussed, the specific impedance bandwidth of an antenna may be calculated.

Again, the impedance bandwidth relates to the frequencies in which the antenna signal may transfer power optimally within reasonable impedance match.

The specification for the GPS bandwidth is mentioned earlier as 2.046MHz.

However, a margin of error will be design to safeguard any drifting of the center frequency. The center frequency due to impedance matching of the Fig. 2-4 antenna is adjusted from the shorting trace of the ‘lowercase h,’ as was for the inverted-f [31]. To ensure a wide range of matching frequencies, a large impedance bandwidth of 300MHz is designed with an ideal center at 1.5754GHz.

Due to the altered square patch portion of the antenna in the proposed design from Fig. 2-4, the square of the antenna height may be determined through [31]

$$BW \cong 50hf^2 \quad (2.38)$$

where h is the height of the patch in cm, f is the frequency in GHz, and BW is the bandwidth in MHz. The height may be determined as

$$h \cong \frac{BW}{50f^2} = \frac{300}{50(1.5754)^2} = 2.419cm .$$

From the grid, the height is rounded down to 2.4 cm. However, a more exact BW is resolved to be

$$BW \cong 50(2.4)(1.5754)^2 = 297MHz .$$

The mentioned calculated bandwidth is in terms of having impedance matching with VWSR equal to 2, in practical terms essentially refers to a return loss, RL, of |-9.5|dB [31].

2.3 Chapter Summary

The inductor theory and analysis has given the background necessary for the design. The two calculation methodologies behind the inductor design were shown, which led to practical calculations. Also, the antenna section described the design methodology as well as the calculation behind the design. Although the antenna design began after the inductors were fully designed, fabricated, and tested, the antenna design is written in this chapter for organization to show the parallels amongst the ideas. The hand calculations that are performed needs to be validated through simulation, which is presented in the next chapter.

3 SIMULATIONS

Simulations are important to verify the calculations and analysis in chapter 2. The simulations would show if the design approximations are feasible. The two simulators that are used are ADS and Sonnet, both softwares are specialized in radio and microwave frequency circuit and components. First the simulations of the two designed inductors are performed and after analysis, the antenna simulations are performed.

3.1 Inductors

In order to simulate the inductors that were designed, layouts must be created in the design tools.

The first layout that is created in ADS is the calculated inductor 'A' with a calculated 55nH for a D_A of 310 mil. Inductor 'A' has metal trace widths of 30 mil wide and 3.5 turns with the determined dimensions shown in Fig. 2-2 and laid out in Fig. 3-1.

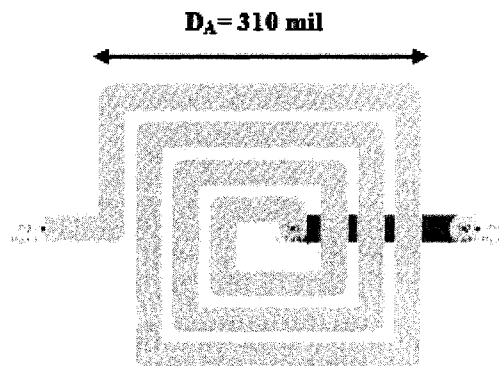


Fig. 3-1 ADS Layout of Inductor 'A'

In Fig. 3-1, the square spiral is drawn with top layer metal with a copper alloy described more in detail in chapter 3 section 2. The small portion near the right feed trace is a bottom trace, which is a necessary bridge underpass to link the two ports of the inductor. Also, two vias are needed to complete the inductor for the two layers. These mentioned characteristics also apply to all the layouts for the inductors in this section.

The layout of inductor 'B' in ADS is for the calculated 100nH inductor. The determined dimensions chapter 2 section 1 shown in Fig. 2-3, where the metal trace width is 60 mil with a spacing of 10 mil with 3.5 turns. The length of each side for the mentioned inductor is $D_B=570\text{mil}$, which was calculated through (2.9) is shown in Fig. 3-2.

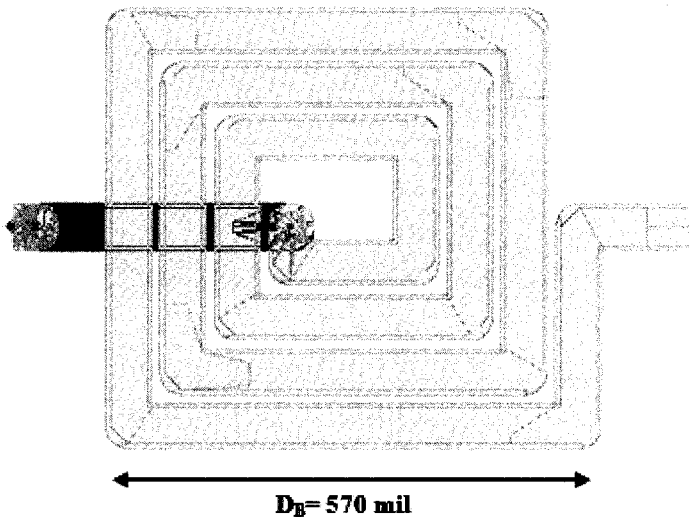


Fig. 3-2 ADS Layout of Inductor 'B'

As the layouts of the calculated inductors are created in ADS, simultaneously two inductors are similarly laid out in Sonnet. Fig. 3-3 shows the layout for the

inductor 'A' design with the width of 30mil, spacing of 10mil, 3.5 turns, and $D_A=310$ mil.

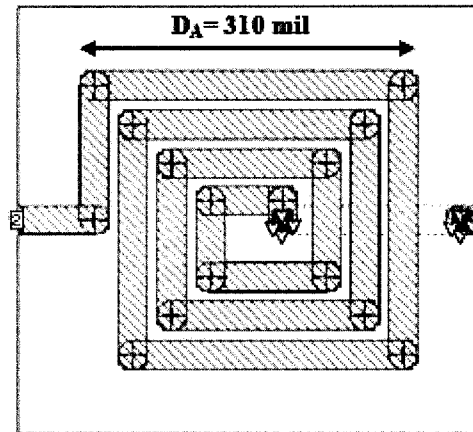


Fig. 3-3 Sonnet Layout of Inductor 'A'

Again, the two vias and the underpass bridge are visible. Inductor 'B' with trace width of 60 mil, spacing of 10 mil, 3.5 turns, and $D_B=570$ mil is shown in Fig. 3-4.

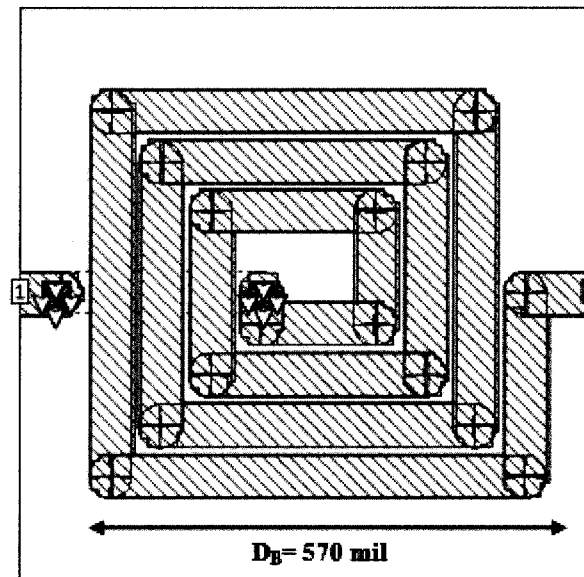


Fig. 3-4 Sonnet Layout of Inductor 'B'

The simulations for both ADS and Sonnet result in S-parameters. Parameters S_{11} , S_{21} , S_{12} , and S_{22} are shown as the results. Both inductor 'A' and inductor 'B' S-parameters are displayed side by side so the differences may be compared. Fig. 3-5 shows S_{11} parameters of the two inductors.

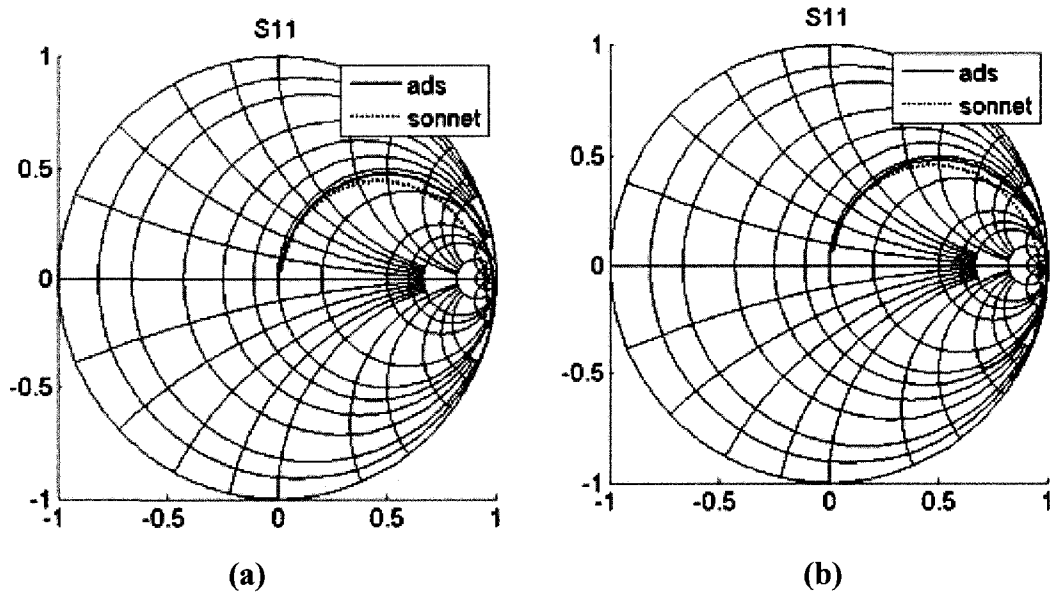


Fig. 3-5 Simulated S_{11} Parameters of (a) Inductor 'A' and (b) Inductor 'B'

The profiles of the simulations in Fig. 3-5(a) are very close between ADS and Sonnet. The same also is true in Fig. 3-5(b). The top portions of the Smith charts in Fig. 3-5 are the inductive regions, while the bottom portions are the capacitive regions. Fig. 3-5 (a) shows the results of the inductor 'A' which is the calculated 55nH inductor designed to have a resonant frequency at 300MHz, while Fig. 3-5 (b) is the inductor 'B' which is the calculated 100nH inductor with a resonant frequency at 200MHz. Both Fig. 3-5 (a) and Fig. 3-5 (b) are simulations of the two inductors up to 1GHz. The point in which the simulation result crosses from the top region to the bottom region occurs later in Fig. 3-5 (a) than in Fig. 3-5 (b), with the understanding that

both frequency limits are the same. Fig. 3-5 (a) and Fig. 3-5 (b) simulation results are expected.

The simulations of S_{21} for both inductor 'A' and inductor 'B' are shown in Fig. 3-6, (a) and (b), which represents the transmitted signal coefficient.

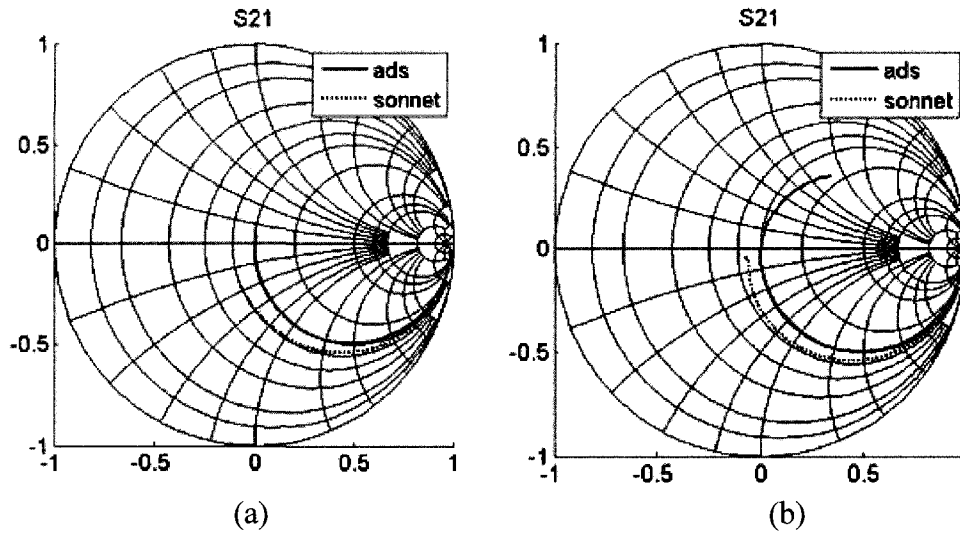
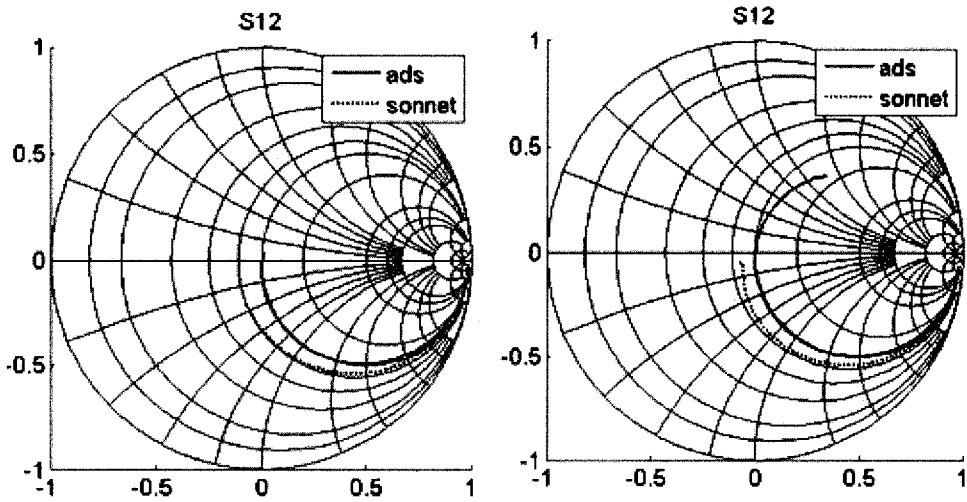
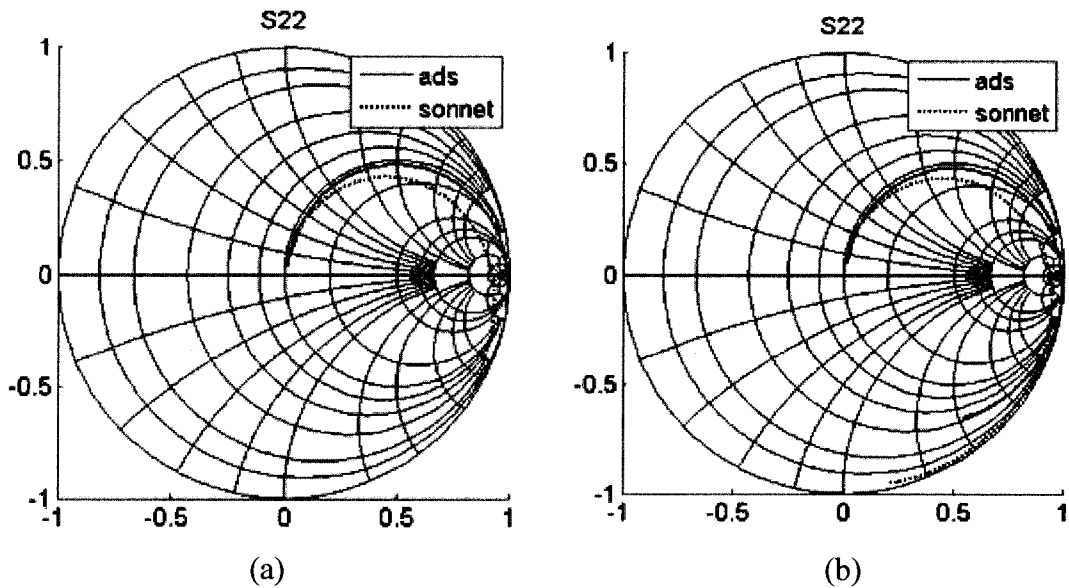


Fig. 3-6 Simulated S_{21} Parameters of (a) Inductor 'A' and (b) Inductor 'B'

The S_{11} and S_{22} parameters represent the reflected signals, while S_{12} and S_{21} represent the transmitted signals. Fig. 3-7 (a) and (b) shows both S_{12} parameters, while Fig. 3-8 (a) and (b) shows the S_{22} simulations for the two designed inductors.



(a) (b)
Fig. 3-7 Simulated S_{12} Parameters of (a) Inductor 'A' and (b) Inductor 'B'



(a) (b)
Fig. 3-8 Simulated S_{22} Parameters of (a) Inductor 'A' and (b) Inductor 'B'

Essentially, the simulation results for the S_{11} are very close to S_{22} due to the symmetrical passive geometry. Similarly the S_{12} and S_{21} are in close agreement in both inductors.

3.1.1 Inductance

The inductances are computed from the raw S parameter data that are converted to Z parameters. From the converted Z-parameters, the inductance with the varying frequency may be determined through the following equation [33]

$$L = \frac{\text{im}\left(Z_{11} - \frac{Z_{12} \times Z_{21}}{Z_{22}}\right)}{2\pi f}, \quad (3.1)$$

where the result is plotted in Fig. 3-9 for the 55nH inductor 'A' and Fig. 3-10 for the 100nH inductor 'B.'

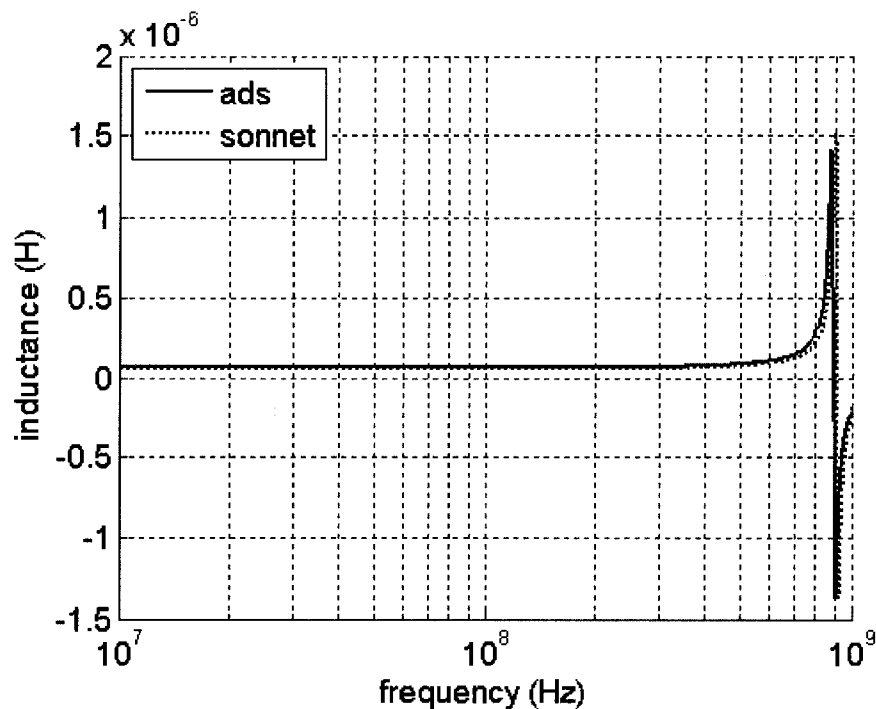


Fig. 3-9 Simulated Inductance of Inductor 'A'

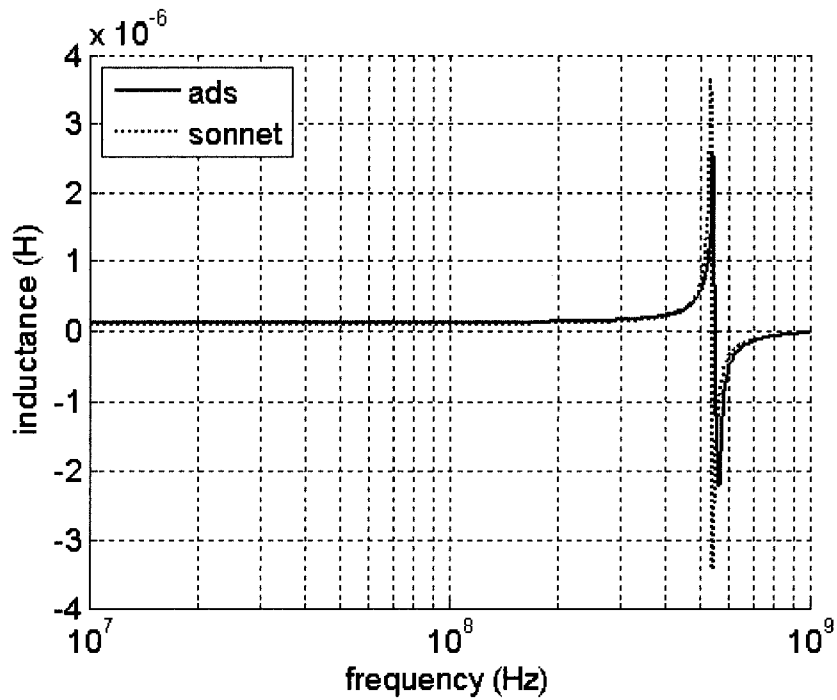


Fig. 3-10 Simulated Inductance of Inductor 'B'

The simulations between ADS and Sonnet for both inductors are reasonably close. The simulated inductor values are close to the calculation values, which will be discussed further in detail in the measurement chapter.

3.1.2 Resistance

The resistance may also be computed from the Z-parameters that was converted from the measured S-parameters in [33]

$$R = \operatorname{re} \left(Z_{11} - \frac{Z_{12} \times Z_{21}}{Z_{22}} \right) \quad (3.2)$$

and plotted in the Fig. 3-11 for the 55nH inductor 'A' and Fig. 3-12 for the 100nH inductor 'B.'

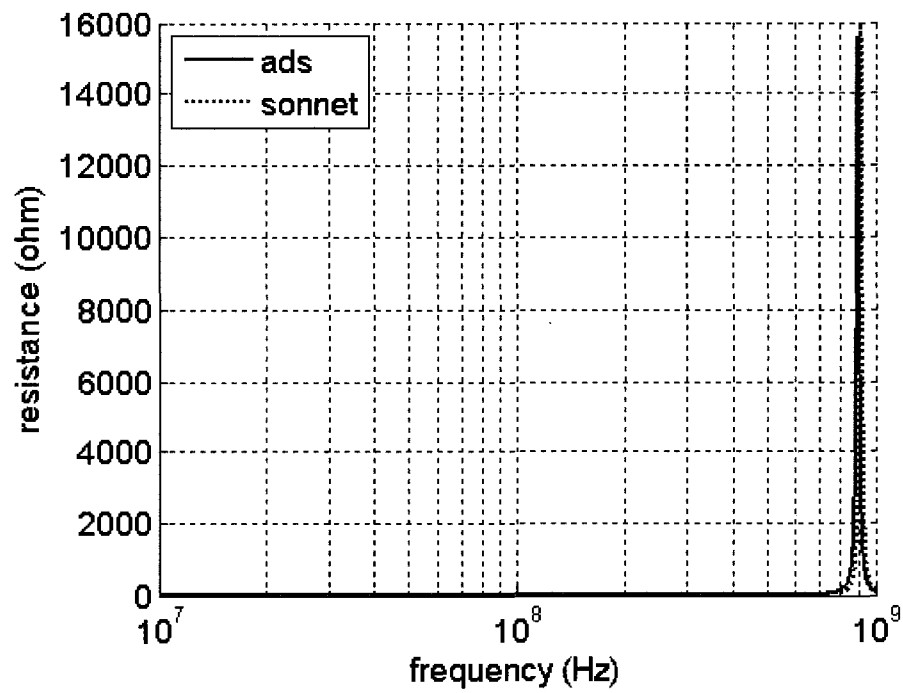


Fig. 3-11 Simulated Resistance of Inductor 'A'

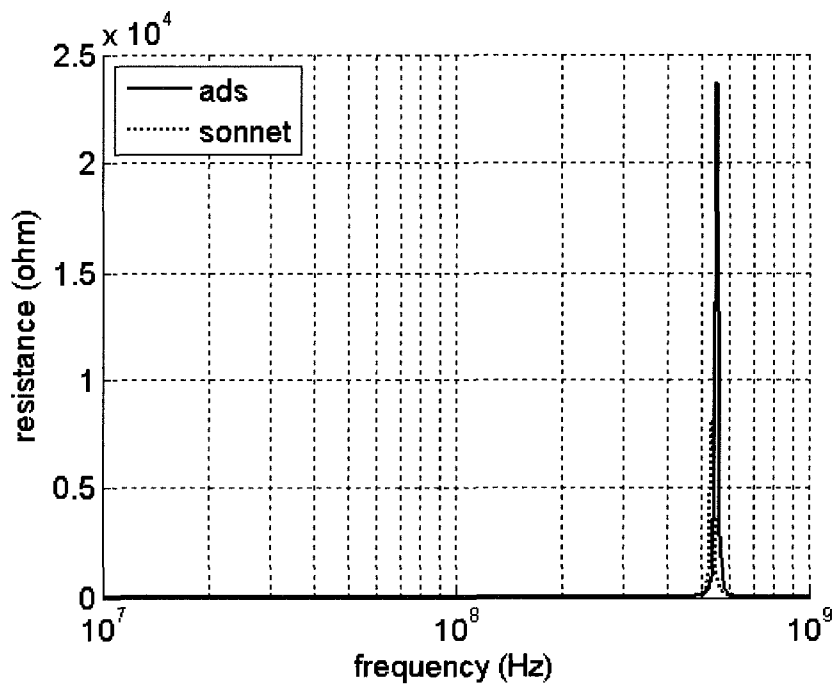


Fig. 3-12 Simulated Resistance of Inductor 'B'

3.1.3 Quality Factor

Finally, the Q-factor may be computed from the measured values through [33]

$$Q = \frac{\text{im} \left(Z_{11} - \frac{Z_{12} \times Z_{21}}{Z_{22}} \right)}{\text{re} \left(Z_{11} - \frac{Z_{12} \times Z_{21}}{Z_{22}} \right)} \quad (3.3)$$

with the results plotted in Fig. 3-13 for the 55nH inductor 'A' and Fig. 3-14 for the 100nH inductor 'B.'

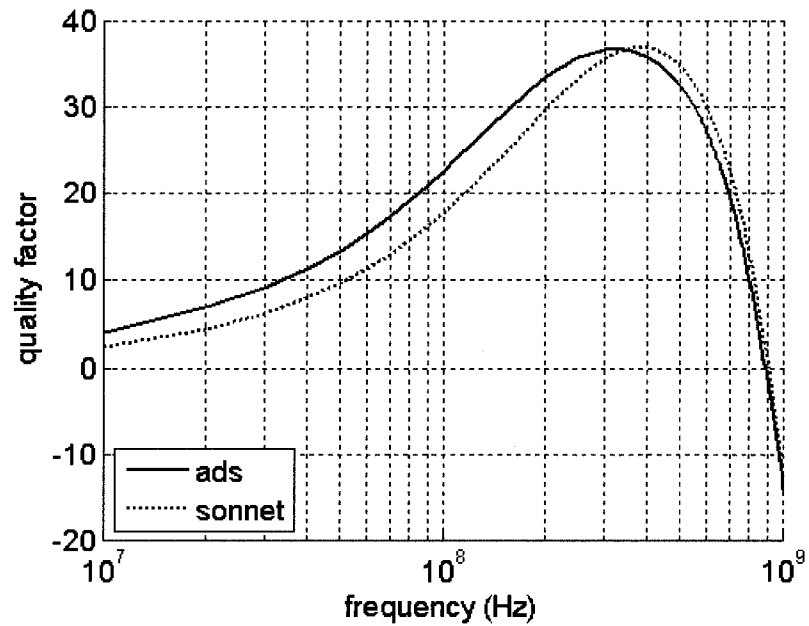


Fig. 3-13 Simulated Resistance of Inductor 'A'

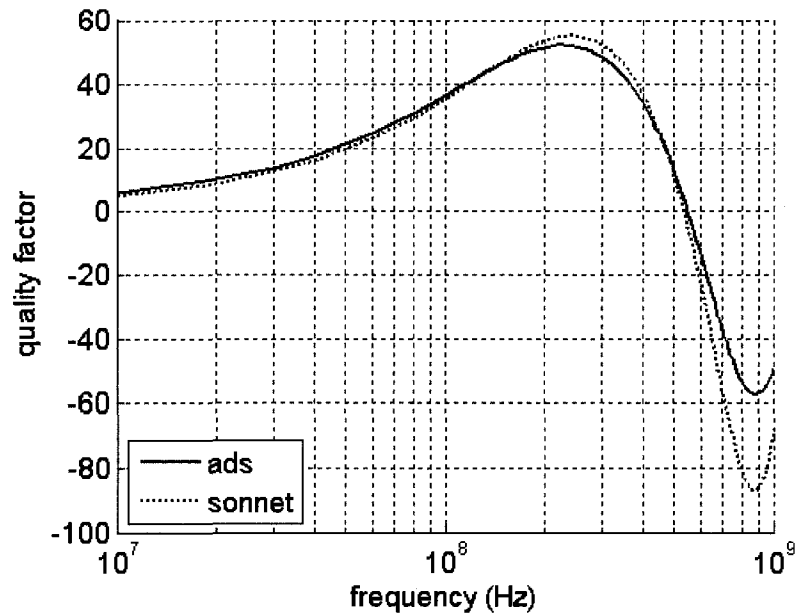


Fig. 3-14 Simulated Resistance of Inductor 'B'

The Q-factor simulations between ADS and Sonnet are close in terms of magnitude and frequency for both inductors, which will further be described with measurements in chapter 4.

3.2 Transition from Inductor to Antenna

The inductor design process is brought forth through calculations, simulations, and measurements, which allowed the characterization of the inductor itself as well as the PCB. PCB characteristics are important which is included in the design flow that will be discussed in detail.

Due to the antennas volatility in frequency and bandwidth profile from manufacturing, two port inductors are a good option for simulator optimization. Through the inductor design process as shown in Fig. 3-15 the simulators are optimized.

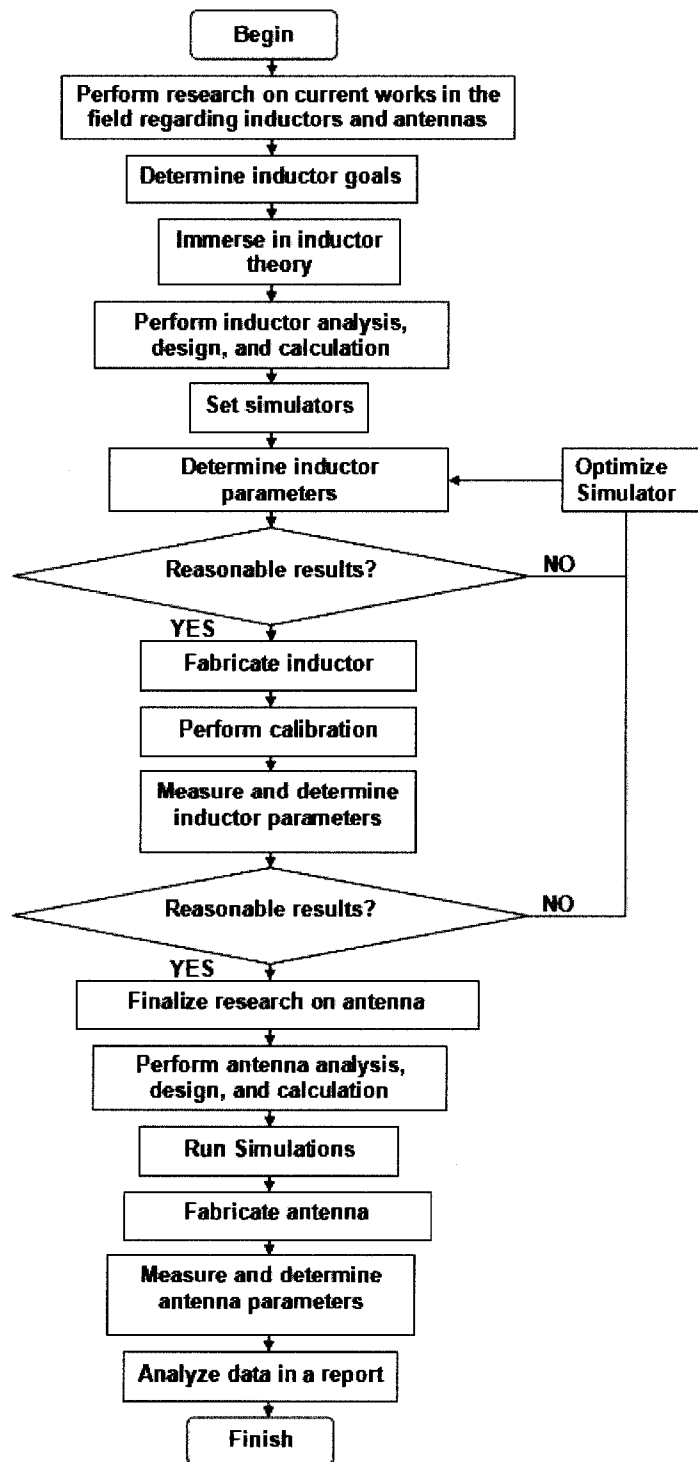


Fig. 3-15 Flow Chart of Design Process

Although the inductors design, fabrication, and measurements are in series to the antenna, this paper explains them in parallel for organization purposes. The flow chart of the proposed design process explains in detail the procedures that are performed. After the whole inductor design flow, inductor characteristics are determined to be used for the antenna design.

The dielectric constant of the FR4 is refined experimentally to be ϵ_r of 3.8. The specified thickness of the substrate is 62.5 mil and the conductor trace thickness 1.4 mil is experimentally determined to be an accurate representation. The original simulations were based on the theoretical conductivity of pure copper to be 5.8×10^7 S/m [23], however through the inductor design flow, as shown in Fig. 3-15, it was discovered that the value was a lower than expected 1.36×10^6 S/m that is found to be optimal for the simulations. With the PCB characteristics determined, the antenna design began.

3.3 Antenna

The simulations for the antenna will begin first with the radiation pattern, directivity and gain, polarization, and impedance bandwidth.

3.3.1 Radiation Pattern

The radiation pattern of the E-field in the phi plane is shown in following figure Fig. 3-16.

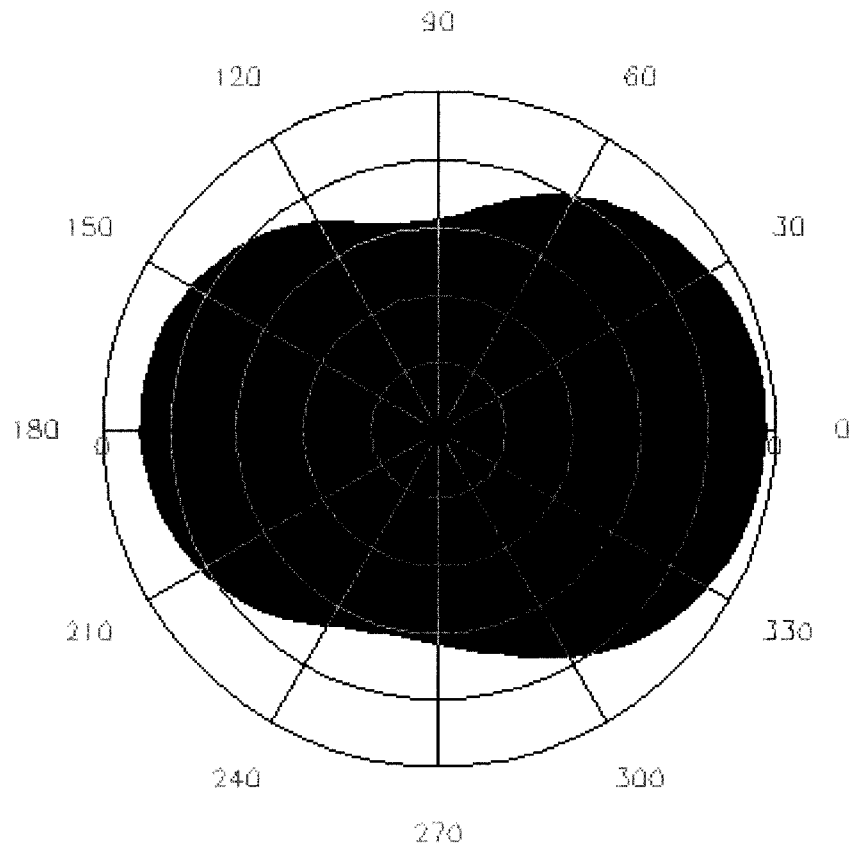


Fig. 3-16 E-field Radiation Pattern

As one may notice, in Fig. 3-16, a main beam exist at 0° created by the reflector. The corresponding maximum intensity in theta is shown in the ADS antenna dialog in Fig. 3-16. From the figure, the beamwidth may also be observed when the field is 3dB from the maximum value in terms of angles, seen to be about 30° each way in this case [11].

3.3.2 Directivity and Gain

The results of the simulation of the ADS antenna dialog are shown in the Table 3-1. The beamwidth is related to the antenna gain and directivity [11]. As with

intuition, beam width is inversely proportional to the gain and directivity, which is high due to the relatively small beamwidth from the previous section.

Table 3-1 ADS Antenna Dialog

ADS Antenna Dialog	
Directivity (dB)	5.0100565
Gain (dB)	5.0031633
Angle of U Max (theta, phi)	72, 0

The theta angle of directivity for the maximum radiation intensity is 72° in as shown in Table 3-1 is 5.01dB. The direction of radiation is the same for the gain, as can be seen in (2.21) and (2.22), which ADS simulation shows the gain to be 5.00dB. This implies very high efficiency with the equation through (2.23).

The theta angle vs. the gain may be displayed in the Sonnet simulation, which shows reasonably similar results regarding the gain at 72° in Fig. 3-17.

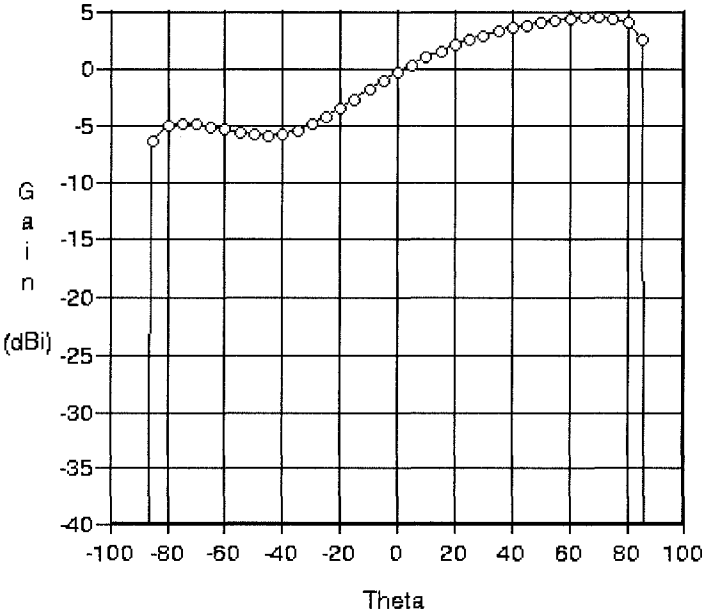


Fig. 3-17 Sonnet Theta vs. Gain

For the design of a portable GPS handheld antenna mounted within the car, the theta angle allows sight to the sky.

3.3.3 Polarization

The simulation of the polarization regarding the radiation is discussed in this section. The single fed cornered patch in Fig. 2-4 helps create right hand circular polarization [34] as shown in Fig. 3-18.

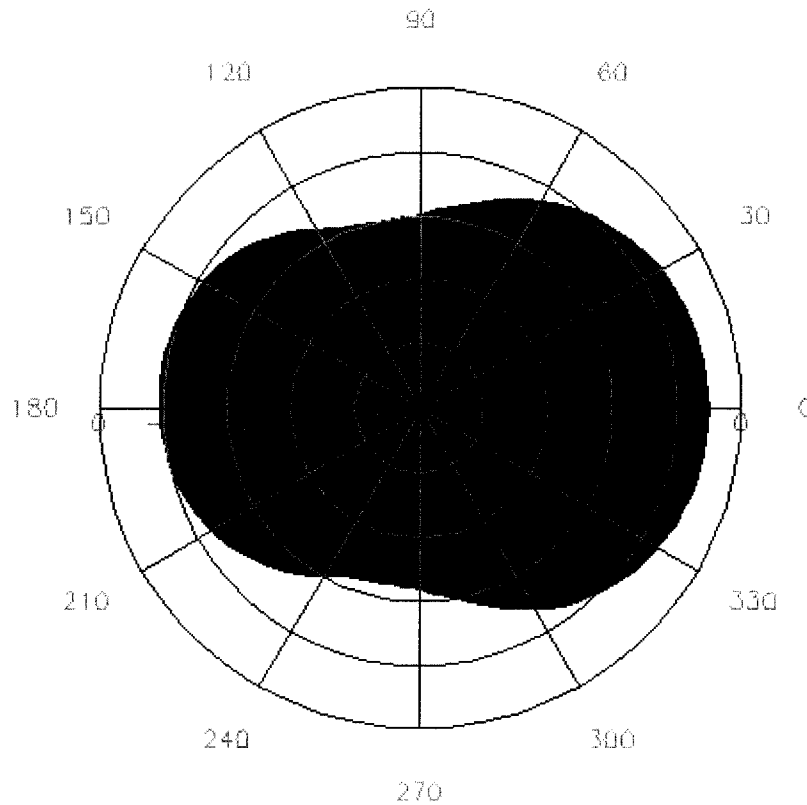


Fig. 3-18 Right Hand Circular Polarization Pattern

The direction of the right hand circular polarization is shown to be at 0° theta in Fig. 3-18 just as the E field in Fig. 3-16.

3.3.4 Impedance Bandwidth

In order to check the resonant frequency and impedance bandwidth profile, the proposed antenna of Fig. 2-4 is simulated in both ADS and Sonnet. Fig. 3-19 shows the S_{11} simulation of the antenna.

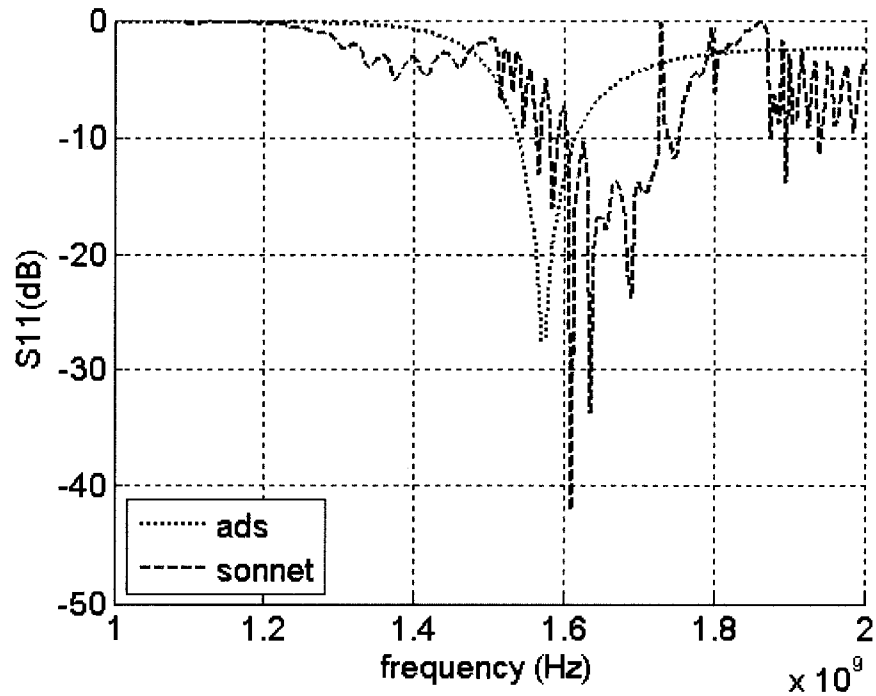


Fig. 3-19 Simulated S_{11} of Antenna Design

As can be seen in Fig. 3-19, both simulations are desirable in terms different aspects, ADS in terms of the resonant frequency and Sonnet in terms of bandwidth.

3.4 Chapter Summary

The simulations show that the design methodology used in chapter 2 were in the correct direction for both the inductors and antenna designs. An important section is the ‘Transition from Inductor to Antenna,’ which is chapter 3 section 2 because the complete design flow is presented in Fig. 3-15. As mentioned in the flow, the next step is to fabricate and measure the designs, which leads to chapter 4, ‘Measurements.’

4 MEASUREMENTS

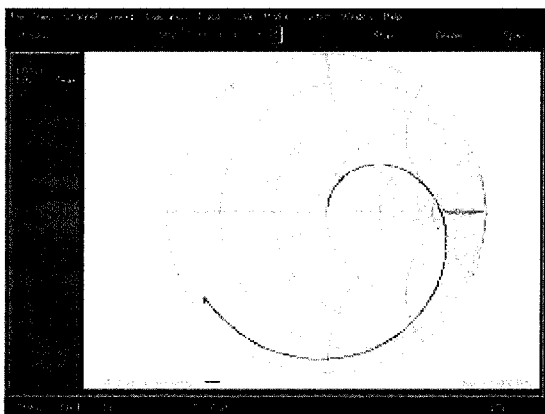
This chapter will cover the conditions of measurements, the calibration and de-embedding, and the measurements for the inductors and antennas.

4.1 Measurement Conditions

To be clear, due to the available resources, the measurements were not performed in an anechoic chamber. Also, the measurements were not performed within an absorbing material box. The measurements were performed in a standard lab environment. Typical ambient environment atmosphere are to be considered with the measurement results.

The measurements are performed with a network analyzer with the device under test. In order to accurately re-plot the digitized data, MATLAB is used. The typical transfer from the instrument data to the PC display is shown in Fig. 4-1.

Network Analyzer



Matlab

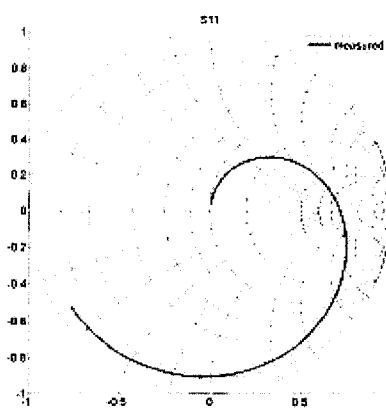


Fig. 4-1 Transfer Data from Network Analyzer to Matlab

4.2 Calibration and De-embedding

For the most accurate results in measurements, both calibration and de-embedding are needed and are discussed in the two following sections.

4.2.1 VNA and Calibration

After fabrication of the PCB inductors, the physical inductors may be measured and compared to the simulated. However, before measurement may take place, calibration is necessary and vital.

The inductors are measured on a network analyzer, and to remove the effects of everything excluding the device under test, DUT, a calibration technique called SOLT meaning short, open, load, thru is performed [35].

To calibrate through the SOLT method, one first physically connects a short connector, an open connector, a load connector, and a thru connector one at a time to both port one and port two of the network analyzer. Essentially the calibration process removes the 12 error terms as shows in the following [36]:

Table 4-1 Twelve Error Terms

	Parameter	Description	Relation to Calibration
Forward	e_{00}	directivity	open
	e_{11}	port 1 match	load
	$e_{10}e_{01}$	reflection	short
	$e_{10}e_{32}$	transmission	thru
	e_{22}	port 2 match	load
	e_{30}	leakage	isolation
Reverse	e'_{33}	directivity	open
	e'_{11}	port 1 match	load
	$e'_{23}e'_{32}$	reflection	short
	$e'_{23}e'_{01}$	transmission	thru
	e'_{22}	port 2 match	load
	e'_{03}	leakage	isolation

The error terms help determine the true four S-parameters of the DUT as shown in the following [36]-[37]:

$$S_{11} = \frac{\left(\frac{S_{11M} - e_{00}}{e_{10}e_{01}} \right) \left[1 + \left(\frac{S_{22M} - e'_{33}}{e'_{23}e'_{32}} \right) e'_{22} \right] - e_{22} \left(\frac{S_{21M} - e_{03}}{e_{10}e_{32}} \right) \left(\frac{S_{12M} - e'_{03}}{e'_{23}e'_{01}} \right)}{\left[1 + \left(\frac{S_{11M} - e_{00}}{e_{10}e_{01}} \right) e_{11} \right] \left[1 + \left(\frac{S_{22M} - e'_{33}}{e'_{23}e'_{32}} \right) e'_{22} \right] - \left(\frac{S_{21M} - e_{30}}{e_{10}e_{32}} \right) \left(\frac{S_{12M} - e'_{03}}{e'_{23}e'_{01}} \right)} \quad (4.1)$$

$$S_{12} = \frac{\left(\frac{S_{12M} - e'_{03}}{e'_{23}e'_{01}} \right) \left[1 + \left(\frac{S_{11M} - e_{00}}{e_{10}e_{01}} \right) (e_{11} - e'_{11}) \right]}{\left[1 + \left(\frac{S_{11M} - e_{00}}{e_{10}e_{01}} \right) e_{11} \right] \left[1 + \left(\frac{S_{22M} - e'_{33}}{e'_{23}e'_{32}} \right) e'_{22} \right] - \left(\frac{S_{21M} - e_{30}}{e_{10}e_{32}} \right) \left(\frac{S_{12M} - e'_{03}}{e'_{23}e'_{01}} \right)} \quad (4.2)$$

$$S_{21} = \frac{\left(\frac{S_{21M} - e_{30}}{e_{10}e_{32}} \right) \left[1 + \left(\frac{S_{22M} - e'_{33}}{e'_{23}e'_{32}} \right) (e'_{22} - e_{22}) \right]}{\left[1 + \left(\frac{S_{11M} - e_{00}}{e_{10}e_{01}} \right) e_{11} \right] \left[1 + \left(\frac{S_{22M} - e'_{33}}{e'_{23}e'_{32}} \right) e'_{22} \right] - \left(\frac{S_{21M} - e_{30}}{e_{10}e_{32}} \right) \left(\frac{S_{12M} - e'_{03}}{e'_{23}e'_{01}} \right)} \quad (4.3)$$

$$S_{22} = \frac{\left(\frac{S_{22M} - e'_{33}}{e'_{23}e'_{32}} \right) \left[1 + \left(\frac{S_{11M} - e_{00}}{e_{10}e_{01}} \right) (e_{11} - e'_{11}) \right]}{\left[1 + \left(\frac{S_{11M} - e_{00}}{e_{10}e_{01}} \right) e_{11} \right] \left[1 + \left(\frac{S_{22M} - e'_{33}}{e'_{23}e'_{32}} \right) e'_{22} \right] - \left(\frac{S_{21M} - e_{30}}{e_{10}e_{32}} \right) \left(\frac{S_{12M} - e'_{03}}{e'_{23}e'_{01}} \right)} \quad (4.4)$$

In subscript of the error terms, 'e', the notation 0 represents port one from the network analyzer side, subscript notation 1 represents port one on the DUT side, subscript notation 2 represents port two on the DUT side, and subscript notation 3 represents the port two the network analyzer side. The subscript 'M' refers to measured S-parameters before calibration.

4.2.2 PCB Trace De-embedding

Similar to the calibration, the effects of the physical connectors as well as the traces between the physical connectors leading to the DUT must be removed. To perform that, a de-embedding process is required. The following equations show the required procedures to determine the true impedance of the inductor [38]:

$$Y_{DUT1} = Y_{DUT} - Y_{OPEN} \quad (4.5)$$

$$Y_{SHORT1} = Y_{SHORT} - Y_{OPEN} \quad (4.6)$$

$$Z_{INDUCTOR} = Z_{DUT1} - Z_{SHORT1} \quad (4.7)$$

As can be inferred through the equations, additional circuits consisting of an open and a short, needs to be added onto the PCB to remove the unwanted effects. The full PCB is shown with the de-embedding circuits shown in Fig. 4-2.

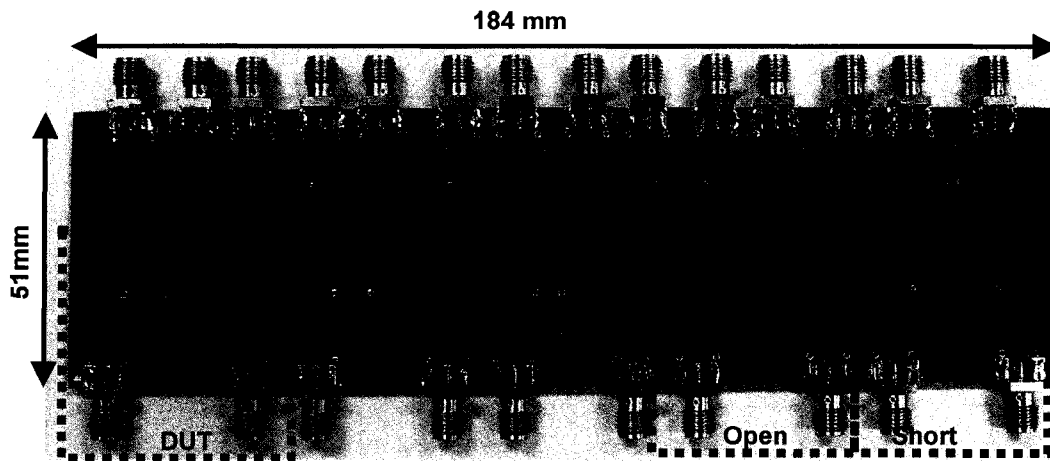


Fig. 4-2 Fabricated Inductors with De-embedding Circuits

The main focus of Fig. 4-2 is the inductor labeled “DUT,” along with the “Open” and “Short” circuits. The other circuits are variations which will later be briefly described.

The de-embedding circuits are very important to remove the unwanted effects, as can be clearly seen in Fig. 4-3 for a particular sample inductor, the raw measured data is corrected with (4.5), (4.6), and (4.7).

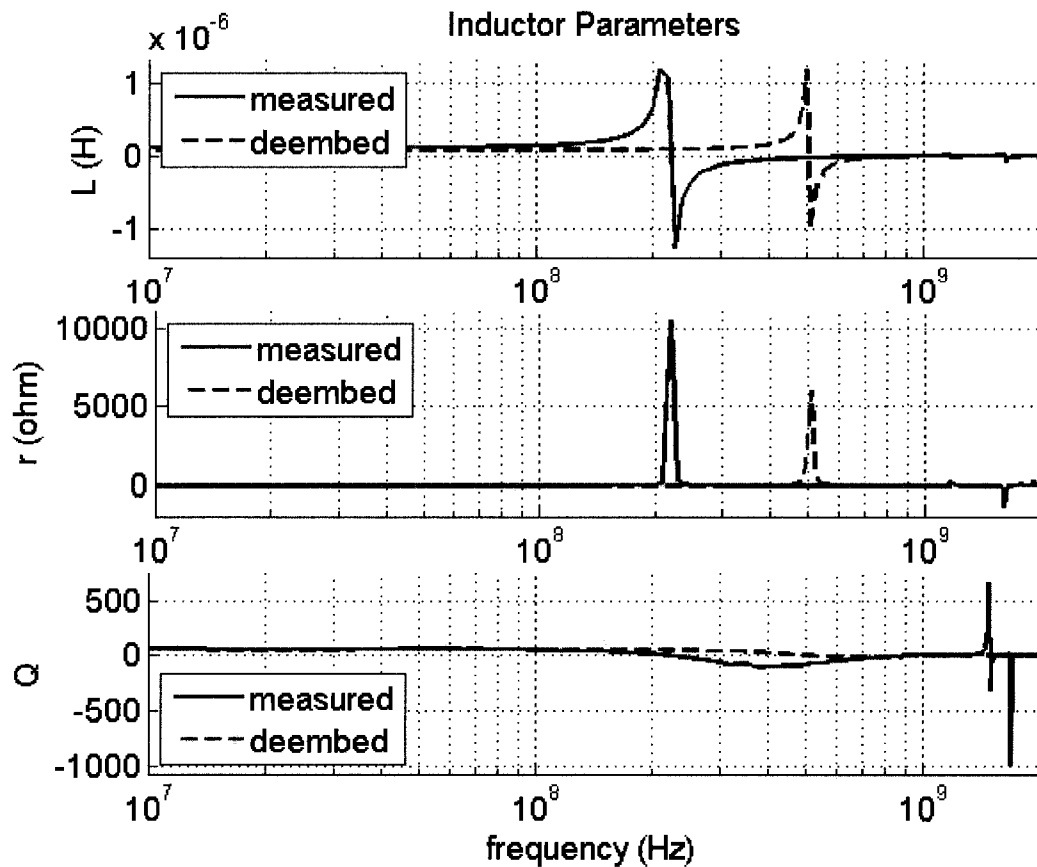


Fig. 4-3 Example of the Effects of Trace De-embedding (Using Open-Shorts)

As can be seen Fig. 4-3, the de-embedding is very useful to show the true inductance, resistance, quality factor, as well as the resonant frequency. Also, Fig. 4-3 shows spikes that are caused by parasitics are removed.

Although originally (4.5), (4.6), and (4.7) works for DUTs that are designed in silicon [38], conceptually the equations also works on PCB circuits. Essentially the de-embedded can be recovered by measuring the non-de-embedded DUT, an open circuit, and a short circuit. The short and open circuits have the lengths of the unwanted traces omitting the DUT. Finally with the measurements acquired, the steps to uncover the impedance characterization are performed through (4.5), (4.6),

and (4.7).

In Fig. 4-2, some interesting conclusions came from designing smaller circuits with longer feed lines relative to the DUT. First by analyzing (4.5) and (4.6), intuitively, one can see that if resistance per square between the feed trace and the DUT are the same, negative impedance may occur if the feed trace length is longer. Through experimentation, (4.5), (4.6), and (4.7) are accurate when the length of open and short feed traces are much smaller relative to the length of the DUT trace.

As an experiment, for example, in Fig. 4-2, the accuracy of the smaller inductors is seen to highly depend on the length of the feed trace to the length of the DUT trace ratio. The DUTs with $N=2.5$ and $N=1.5$ turns for both 30 mil and 60 mil trace widths were less accurate than the $N=3.5$, 30 mil and 60 mil circuits. After further analysis, the DUT of $N=3.5$ with 60 mil width has higher accuracy than the $N=3.5$ with 30 mil width. The reason is because the $N=3.5$ with 60 mil has an innately longer DUT trace than the 30 mil DUT trace relative to the same feed traces. Experimentally, when the feed trace was less than 13.9% of the DUT trace, the results were much more accurate. The smaller the percentage of feed traces relative to the DUT traces the better.

The whole process of calibration and de-embedding ensures confidence in the measurements. From this point on in the next sections, the “measured” results are regarding the inductors that have been de-embedded.

4.3 Inductors

For the fabrication, an actual layout must be created to be manufactured. In addition to the inductors, pads for measurement connectors as well as a clear ground connection must be ensured. The two layouts, inductor 'A' and inductor 'B' are shown in Fig. 4-4 and Fig. 4-5, respectively.

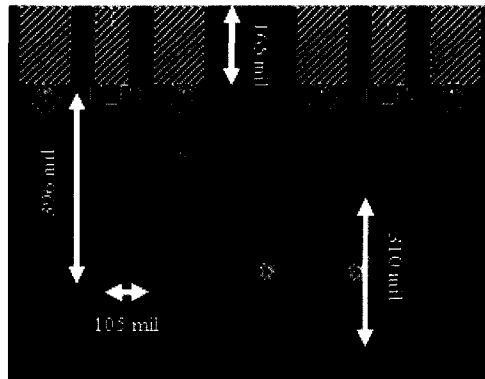


Fig. 4-4 Layout for Fabrication for Inductor 'A'

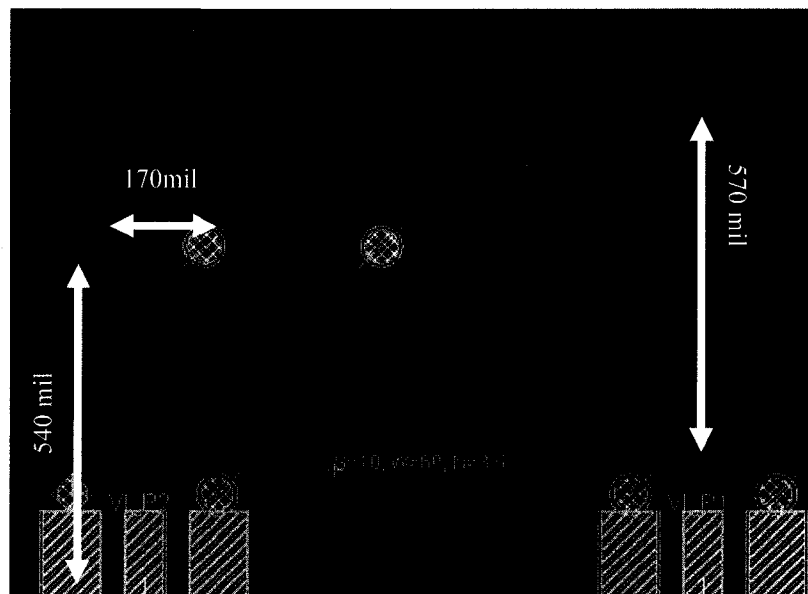


Fig. 4-5 Layout for Fabrication for Inductor 'B'

The detailed dimensions for Fig. 4-4 are shown in Fig. 2-2 and the detail dimensions

for Fig. 4-5 are shown in Fig. 2-3.

After performing calibration and de-embedding, the measurements for the inductors are performed. The measured values of DUT from the network analyzer are converted into MATLAB for comparison purposes.

The measured inductor S_{11} parameters with inductor trace width of 30 mil and 60 mil are shown in Fig. 4-6 (a) and Fig. 4-6 (b), which are shown of the along with the simulated results from ADS and Sonnet.

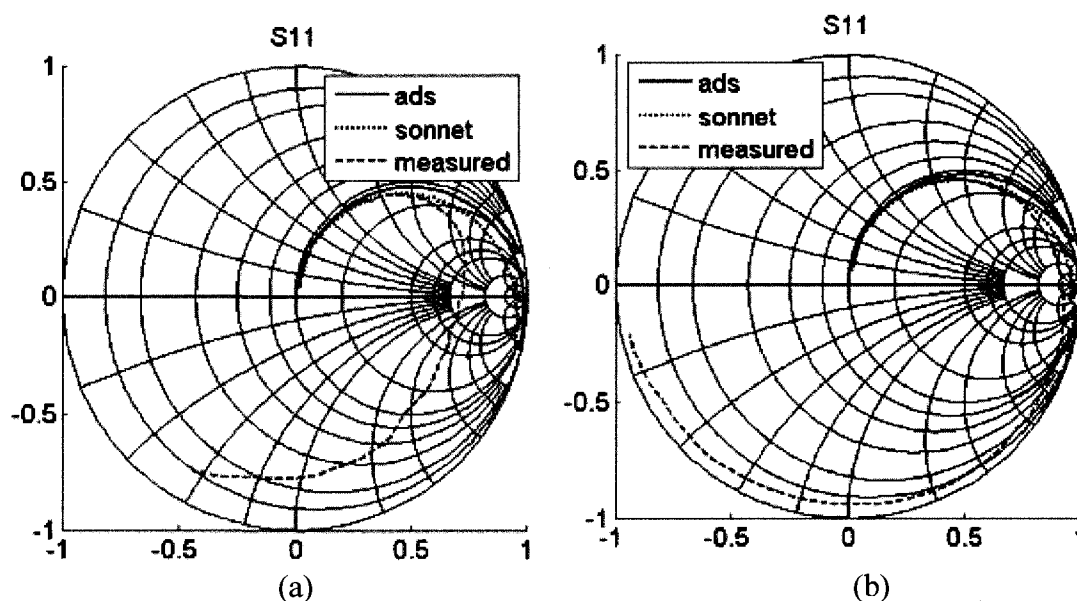


Fig. 4-6 Measured S_{11} Parameters of (a) Inductor 'A' and (b) Inductor 'B'

Through observation, the first part of the measurements at very low frequencies follows the simulated; however, the overall profile of Fig. 4-6 (b) provides much better results in terms of the trend due to the limits of de-embedding. The shorter inductor 'A' DUT trace length is noticeable with the unusual phenomenon in the transmission coefficient, S_{12} in Fig. 4-7 (a). Figure 4-7 (b) due to the larger DUT trace length to feed trace ratio is clear that the results are more accurate as expected.

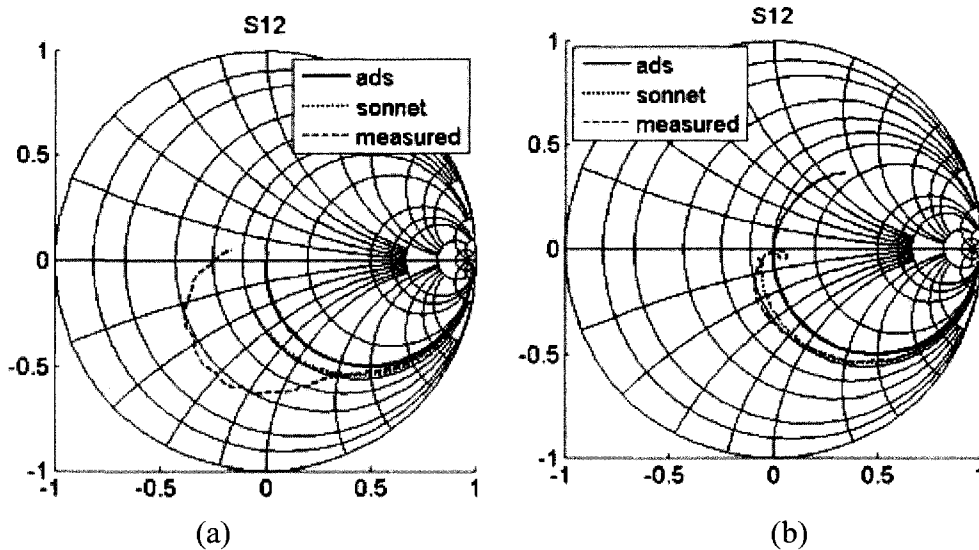


Fig. 4-7 Measured S_{12} Parameters of (a) Inductor 'A' and (b) Inductor 'B'

S_{12} corresponds to S_{21} shown in Fig. 4-8 and S_{11} corresponds to S_{12} shown in Fig. 4-9.

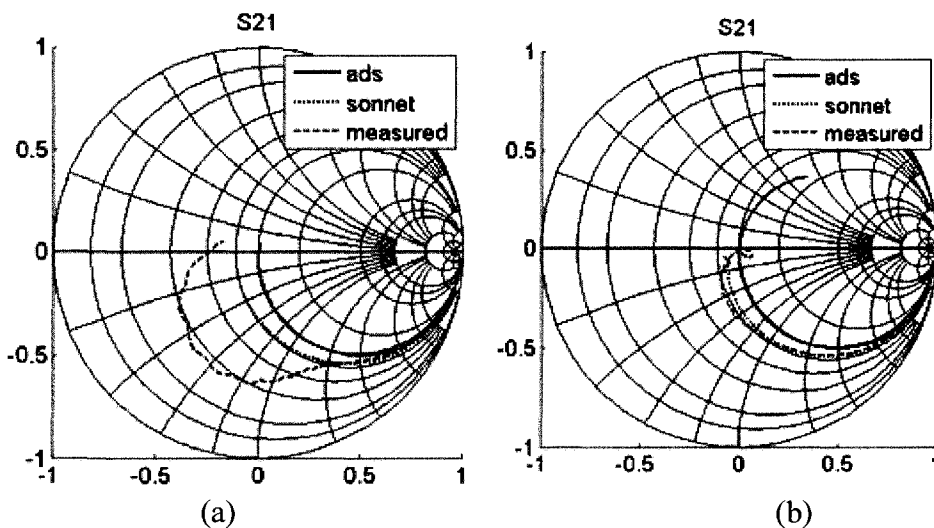


Fig. 4-8 Measured S_{21} Parameters of (a) Inductor 'A' and (b) Inductor 'B'

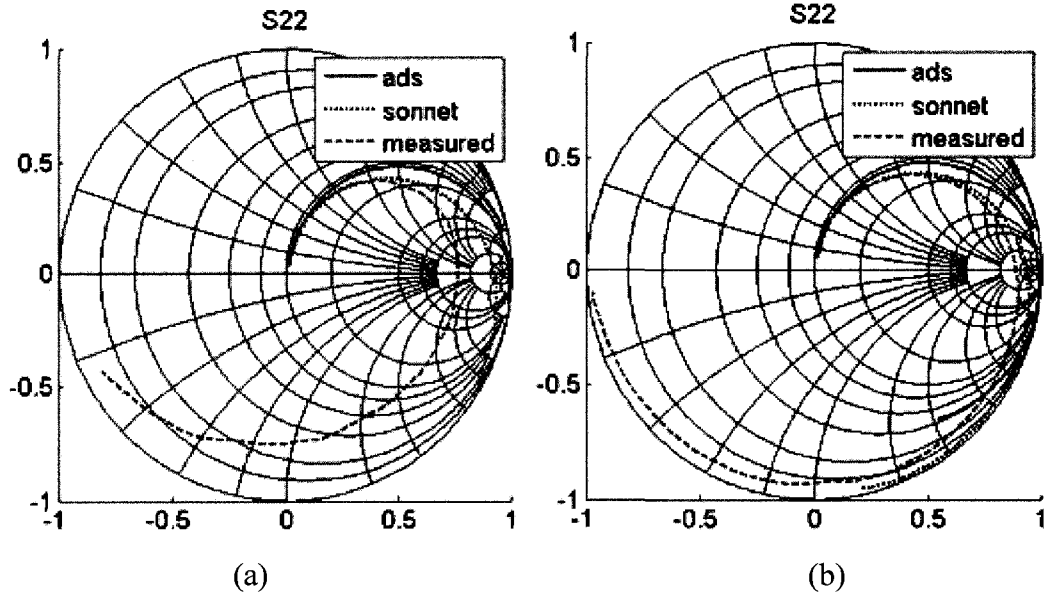


Fig. 4-9 Measured S_{22} Parameters of (a) Inductor 'A' and (b) Inductor 'B'

Through observation, geometrically the S-parameters are similar in both directions, from port one and port two, in terms of S_{11} , S_{12} , S_{21} , and S_{22} .

After S-parameters are measured, the inductance, resistance, quality factor needs to be determined. Through the conversion of the S-parameters to Z-parameters, the three mentioned parameters may be determined.

4.3.1 Inductance

The inductance of inductor 'A' is determined from the converted Z-parameters as in the simulation chapter 3 with calculation of (3.1). Fig. 4-10 shows the result of the calculation and the plot.

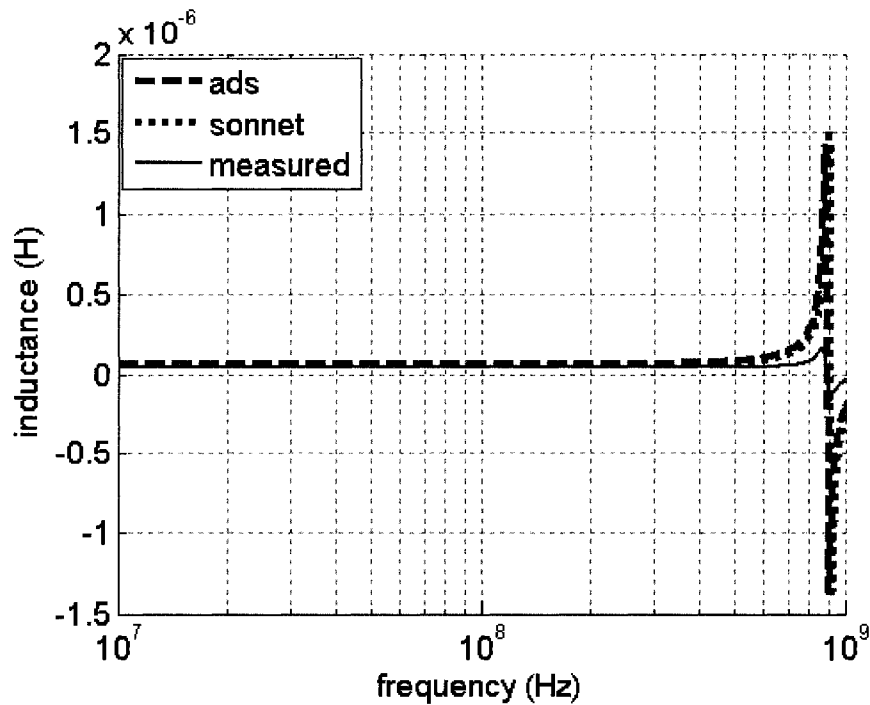


Fig. 4-10 Measured Inductance of Inductor ‘A’ Relative to Simulations

The measurement result that is shown in Fig. 4-10 in relation to the simulations shows that overall the inductance is much lower.

Inductor ‘B’ in Fig. 4-11, the measured peak inductance occurs slightly before the simulation peak does, however, the overall the inductance value follows the simulation as seen by the overlap from most of the frequency range. The inductance at the operating frequency, 200MHz, is more important than the actual resonant frequency, which is close to the simulations and calculations. A tabulated at the end of the chapter will summarize the results.

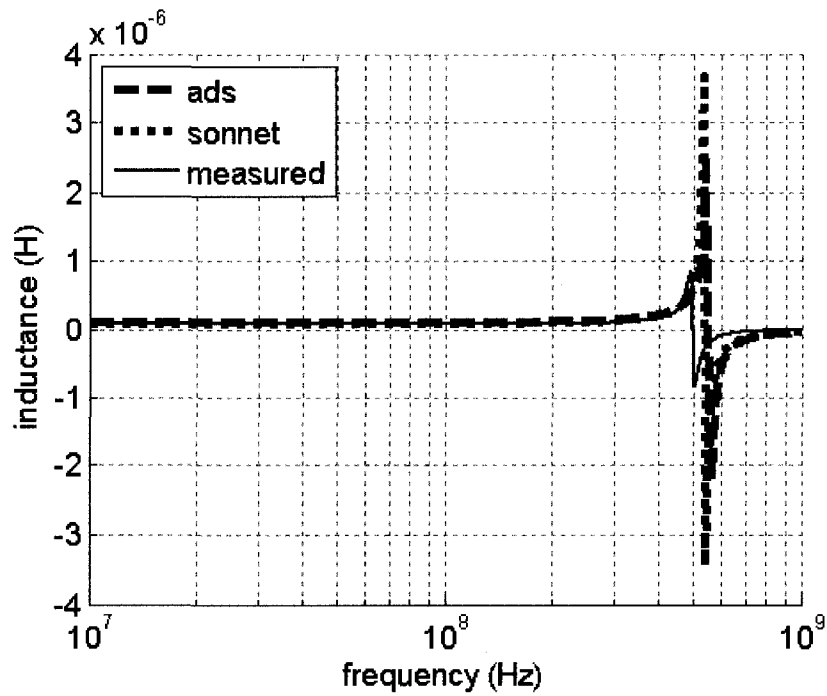


Fig. 4-11 Measured Inductance of Inductor ‘B’ Relative to Simulations

With the inductances for both inductors presented, the resistance will be discussed.

4.3.2 Resistance

The internal series resistances of the two inductors are calculated from the converted Z-parameters through (3.2). The measurement for inductor ‘A’ is shown in Fig. 4-12, while the measurement for inductor ‘B’ is shown in Fig. 4-13.

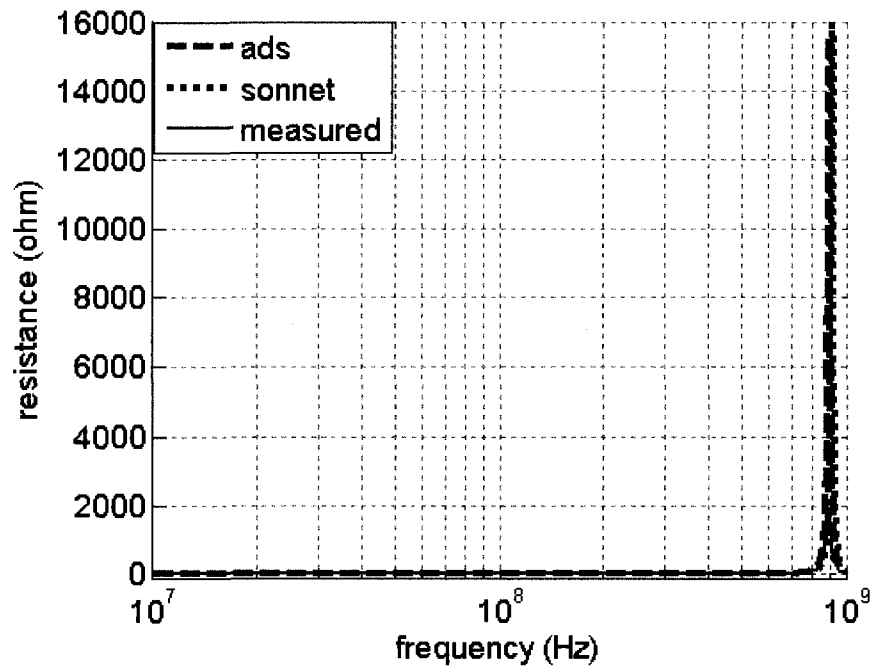


Fig. 4-12 Measured Resistance of Inductor 'A' Relative to Simulations

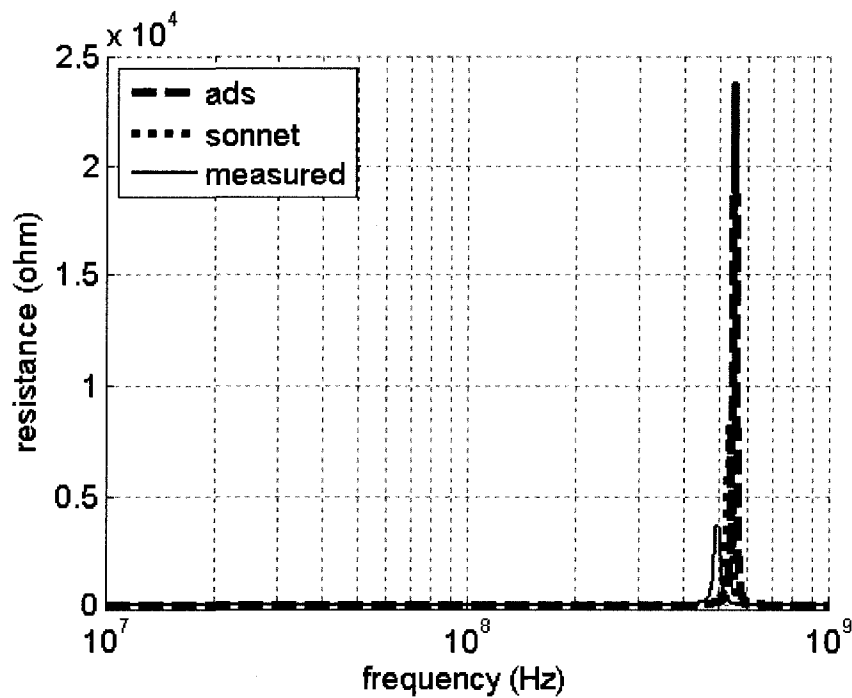


Fig. 4-13 Measured Resistance of Inductor 'B' Relative to Simulations

When comparing the two figures, Fig. 4-12 and Fig. 4-13, the first figure, inductor 'A' seems to be following the overall profile. However, in further inspection, although the peaks are offset, the inductor 'B' from Fig. 4-13 has also a fairly close resistance at its operating frequency. The spike of resistance occurs because at the resonant frequency, the inductor becomes an open circuit. The results of the inductors will be presented after determining the Q-factor.

4.3.3 Quality Factor

The Q-factor, quality factor, gives the capability to compare two different inductors. The Q-factor may be determined with (3.3) from the converted Z-parameters. The measured Q-factor of inductor 'A' is presented in Fig. 4-14, while the Q-factor of inductor 'B' will be presented in Fig. 4-15.

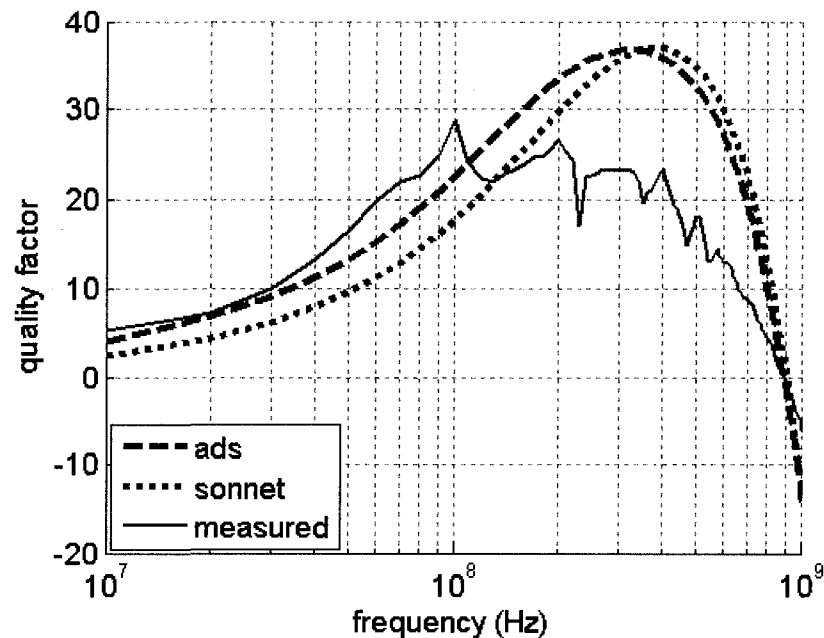


Fig. 4-14 Measured Q-factor of Inductor 'A' Relative to Simulations

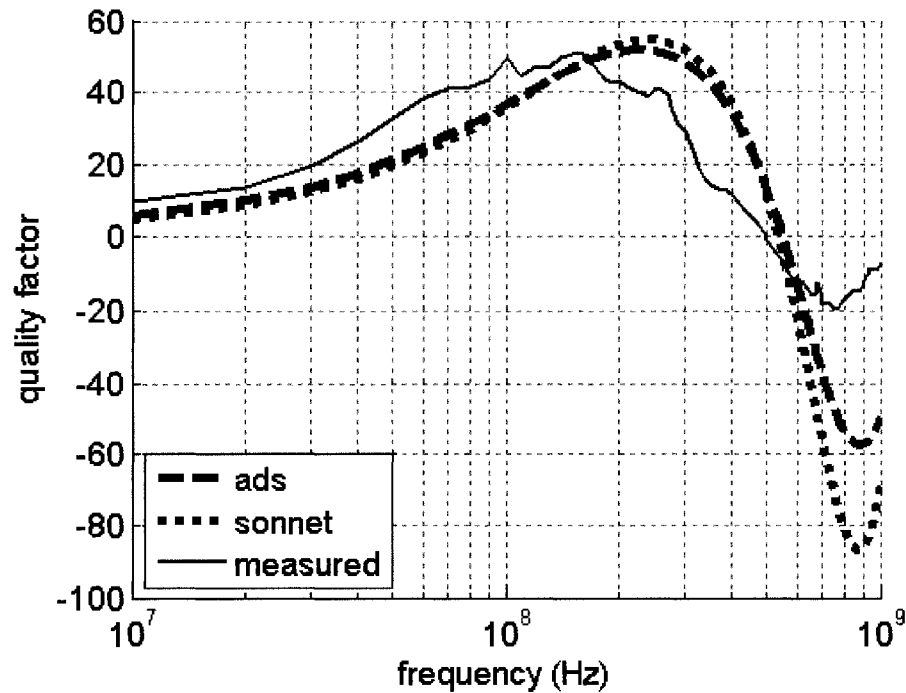


Fig. 4-15 Measured Q-factor of Inductor 'B' Relative to Simulations

From the presented results of the Q-factor in Fig. 4-14 shows to be less accurate as Fig. 4-15, which highly agrees with both simulators. Further comparison of all the results will be shown together in the next section.

4.3.4 Results

The results of both inductors 'A' and 'B' are presented in terms of the calculated values, the both ADS and Sonnet simulations, and the measured. First inductor 'A' will be shown in Table. 4-2.

	Calculated	ADS	Sonnet	Measured
L	55nH	66nH	60nH	45nH
R	3.10Ω	3.95Ω	4.05Ω	4.1Ω
Qmax	33	37	36	29

The measured Q-factor from inductor ‘A’ are quite smaller than the calculated and simulations. The less than expected Q-factor is due to the smaller inductance, which is related to the feed trace to DUT trace ratio. Better results arise from inductor ‘A,’ which has a smaller feed trace to DUT trace ratio, shown in the result summary in Table 4-3.

Table 4-3 Inductor ‘B’ Parameter Summary

	Calculated	ADS	Sonnet	Measured
L	100nH	119nH	101nH	95nH
R	2.38Ω	3.2Ω	2.85Ω	2.9Ω
Qmax	53	52	55	51

The table of summarized values in Table 4-3 shows that the inductance, resistance, and Q-factor are all within reasonable agreement to the simulations, calculations, as well as the design specification.

4.4 Transition from Inductor to Antenna

The inductor began with the design and simulation, which led to the fabrication, and ended with the measurement. The whole flow and process is described in Fig. 3-15. The same process is also true with the antenna, where the measurements will be described after fabrication.

4.5 Antenna

The fabricated GPS antenna of “L-ground plane with lowercase-h configuration and cornered patch” is shown in Fig. 4-16. The figure shows the front and back of the fabricated antenna.

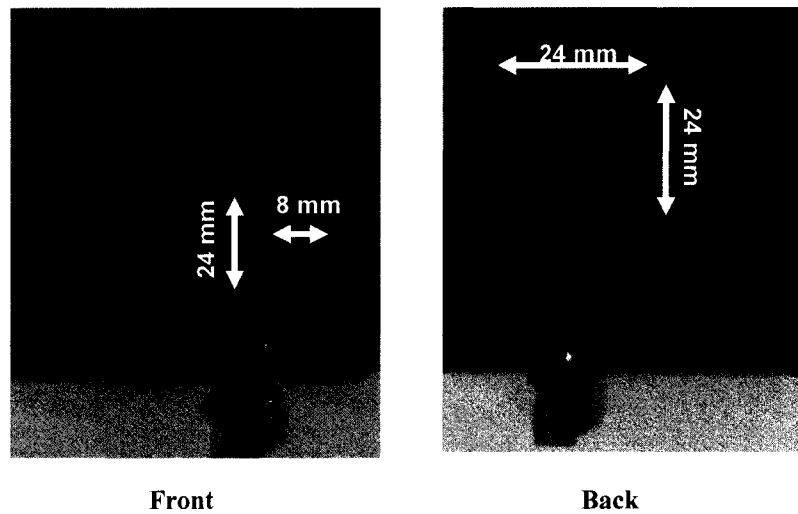


Fig. 4-16 Front and Back Pictures of L-ground Plane with Lowercase-h Configuration and Cornered Patch

Due to the availability of measurement resources, the radiation patterns are only simulated; however, the impedance matching and bandwidth are both simulated and measured.

4.5.1 Impedance Matching

The input impedance is important for maximum power transferred to the antenna. The impedance is matched not only for a particular frequency, but also for a range where the bandwidth is associated with the matching capability. The simulated and measured S_{11} results are shown in Fig. 4-17.

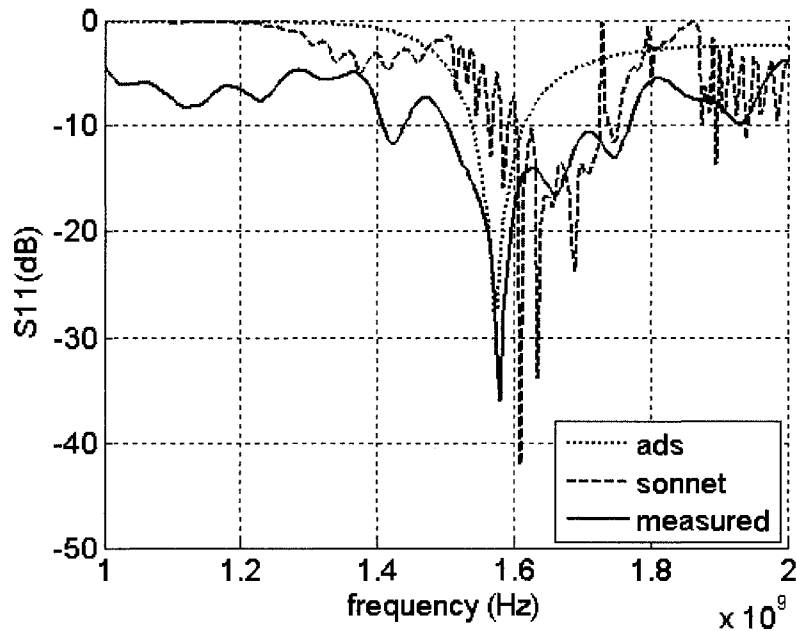


Fig. 4-17 Measured S_{11} Parameter Relative to Simulations

Fig. 4-17 shows that the resonance frequency as well as the bandwidth is within reasonable range of the simulations.

4.5.2 Results

The results of the antenna measurements are tabulated and summarized in Table 4-4 as follows:

Table 4-4 Summary of Impedance Matching and Bandwidth				
	Goal	ADS	Sonnet	Measured
Δ from center	0	4MHz	25MHz	6MHz
BW	297MHz	75MHz	210MHz	250MHz

Both simulators are close to the measured results in different characteristics. In terms of the center frequency, ADS was close, and in terms of the bandwidth profile, Sonnet was close.

Overall, both simulators are important to be used at the same time because

they show different aspects of the device designs, which better predicts the results.

The measured antenna result at 1.5754GHz is -36dB , which is sufficient to the GPS specifications.

4.6 Chapter Summary

This chapter has shown the measurement results for both the inductors and the antennas, which are reasonable. As can be seen, the second inductor, which has physically longer component traces relative to the feed trace, has provided more accurate results, which had helped to characterize the PCB for antenna. With the complete design flow complete, the thesis will be concluded in the next chapter.

5 CONCLUSION

This thesis has shown the full flow starting from designing inductors to designing antennas through PCB board characterization process. This thesis has fully explained the background of inductors and antennas as well as the current field work in the introduction. Next, the theory, analysis, and design chapter has addressed and organized the essential design parameters. With the design thought process well defined, simulations are performed in both ADS and Sonnet, which verifies the expected parameters from the design chapter. To determine the practically, the circuit boards are fabricated and measured which showed that the design calculations and simulations were valid.

The presented design flow determined very good results in terms of the larger inductor and the antenna. The larger 100nH inductor, earlier denoted as inductor 'B,' was much better than the 55nH inductor, earlier denoted as inductor 'A,' as mentioned in chapter 4 section 1.2, due to the ratio of the inductor component's trace length relative to the feed trace length. Relative to the calculations, ADS simulations, Sonnet simulations, the measured inductor 'A' Q-factor value varied from as much as 27.57% to down to 10.34%, while the Q-factor for inductor 'B' value varied from as much as 7.84% to as little as 1.96%. This shows that as long as the inductor component trace is reasonably long relative to the feed, the results will be accurate. The accuracy helps to determine the PCB characteristics such as the dielectric constant, the substrate thickness, and the trace thickness. The results of the antenna after the modeled PCB characteristics resulted in a final center frequency of

1.5814GHz compared to the 1.5754GHz theoretical and 250MHz bandwidth compared to the desired 297MHz. Considering even small manufacturing variations create drastic antenna characteristic results, the measured results are good. Also, the help of the initial inductor design processes increased accuracy in terms of expected variations from optimizing the simulators.

The significance of this thesis is that it shows a student or one who may be interested in antenna design a flow using any available PCB fabrication process. Through the proposed method used is described with inductors essential to radio frequency and microwave that began the design flow. The presented design flow is a valuable contribution to academia.

This project may be extended in the future. First, analyzing the components in an anechoic would be very helpful in further analysis. Secondly, an extension would be to determine the upper limitations of the correlations between the inductor and antenna in terms of frequencies and size. Lastly, higher inductance planar inductors with various cores may be experimentally performed.

References

- [1] H. D. Young and R. A. Freedman, *University Physics with Modern Physics*, San Francisco: Addison Wesley Longman, 2000.
- [2] J. Sevick, *Transmission Line Transformers*, Newington: American Radio Relay League, 1987.
- [3] S. Sridharan, W. Grande, and P.R. Mukund, "High Q embedded inductors in silicon for RF applications," *IEEE International ASIC/SOC Conference*, pp. 346-349, Sept. 2002
- [4] H. Ronkainen, H. Kattelus, E. Tarvainen, T. Ruhissari, M. Andersson, and P. Kuivalainen, "IC Compatible planar inductors on silicon," *IEE Proceedings-Circuits, Devices and Systems*, vol. 144, no. 1, pp. 29-35, Feb. 1997.
- [5] E. Ragonese, T. Biondi, A. Scuderi, and G. Palmisano, "A lumped scalable physics-based model for silicon spiral inductors" *The 10th IEEE International Symposium on Electron Devices for Microwave and Optoelectronic Applications*, pp. 119-124, Nov. 2002.
- [6] T.-P. Wang, H. Wang, "High-Q Micromachined Inductors for 10-to-30GHz RFIC Applications on Low Resistivity Si-Substrate" *36th European Microwave Conference*, pp. 56-59, Sept. 2006.
- [7] J.R. Long and M.A. Copeland, "The modeling, characterization, and design of monolithic inductors for silicon RF IC's," *IEEE Journal of Solid-State Circuits*, vol. 32, no. 3, pp. 357-369, Mar. 1997.
- [8] S. Staff, "Printed Inductors in RF Consumer Applications," *IEEE Trans. on Consum. Electron.*, vol. 47, no. 3, pp. 426-435, Aug 2001.
- [9] C.P. Yue and S.S. Wong, "Physical modeling of spiral inductors on silicon," *IEEE Transactions on Electron Devices*, vol. 47. no. 3, pp. 560-568, Mar. 2000.
- [10] J. L. Sinclair, *How Radio Signals work*, Australia: McGraw-Hill Book Company Australia Pty Limited, 1997.
- [11] R. Garg, P. Bhartia, I. Bahl, and A. Ittipiboon, *Microstrip Antenna Design Handbook*, Norwood: Artech House, Inc., 2001.

- [12] Stanford Report, "GPS inventor inducted into hall of fame," <http://news-service.stanford.edu/news/2004/february18/parkinson-218.html>, Feb. 18, 2004.
- [13] International information programs – Current Issues, "United States Updates Global Positioning System Technology," Feb. 3, 2006. [Online]. Available: <http://usinfo.state.gov/gi/Archive/2006/Feb/06-791119.html>
- [14] *Global Positioning System Standard Positioning Service Standard*, Oct. 2001. [Online]. Available: <http://www.navcen.uscg.gov/gps/geninfo/2001SPSPPerformanceStandardFINAL.pdf>
- [15] M.K. Alsliety and D.N. Aloï, "A Study of Ground-Plane-Level and Vehicle-Level Radiation Patterns of GPS Antenna in Telematics Applications," *IEEE Antennas and Wireless Propag. Lett.*, vol. 6, pp. 130-133, 2007.
- [16] R. Li, B. Pan, J. Laskar, and M.M. Tentzeris, "A Compact Broadband Planar Antenna for GPS, DCS-1800, IMT-2000, and WLAN Applications," *IEEE Antennas and Wireless Propag. Lett.*, vol. 6, pp.25-27, 2007.
- [17] Y. Zhou, C.-C. Chen, and J.L. Volakis, "Dual Band Proximity-Fed Stacked Patch Antenna for Tri-Band GPS Applications," *IEEE Trans. Antennas Propag.*, vol. 55, no. 1, pp. 220-223, Jan. 2007.
- [18] R. A. Serway and R. J. Beichner, *Physics for Scientists and Engineers*, 5th ed. Orlando: Saunders College Publishing, 2000.
- [19] C.K. Alexander and M. N. O. Sadiku, *Fundamental of Electric Circuits*, 2nd ed. New York: McGraw-Hill, 2004.
- [20] H. M. Greenhouse, "Design of Planar Rectangular Microelectronic Inductors," *IEEE Trans. on Parts, hybrids, and Packaging*, vol. 10, no. 2, pp. 101-109, Jun. 1974.
- [21] W.B. Kuhn, A. Elshabini-Riad, and F.W. Stephenson, "Centre-tapped spiral inductors for monolithic bandpass filters," *IEE Electron. Lett.*, vol. 31, no. 8, pp. 625-626, Apr. 1995
- [22] C. R. Paul, "Transmission Lines and Signal Integrity" *Introduction to Electromagnetic Compatibility*, 2nd ed. New Jersey: John Wiley & Sons, Inc., 2006, ch. 4, sec. 5, pp. 274-275.
- [23] D. M. Pozar, *Microwave Engineering*, 3rd ed. New Jersey: John Wiley & Sons, Inc., 2005.

- [24] I. Sinclair, "Inductors and inductive components," *Passive Components for Circuit Design*, Woburn: Newnes, 2001, ch. 5, pp. 134-135.
- [25] Q. Zhu, K. Fu, and T.-Z. Liang, "Analysis of planar inverted-F antenna using equivalent models," *2005 IEEE Antennas and Propagation Society International Symposium*, vol. 3A, pp. 142-145, Jul. 2005.
- [26] G. Qasim, W. Zhao, and J. Zhang, "Inverted F-antenna for mobile communication," *AMPC 2005 Microwave Conference Proceedings*, vol. 5, pp. 4, Dec. 2005.
- [27] V. F. Fusco, *Foundations of Antenna Theory and Techniques*, Essex: Pearson Education Limited, 2005.
- [28] *Advanced Design System Documentation*, Agilent Technologies, Santa Clara, CA, 2004A, ch. 9 pp. 1-12.
- [29] D. K. Cheng, "Plane Electromagnetic Waves," *Fundamentals of Engineering Electromagnetics*, New Jersey: Prentice-Hall, Inc., 1993, ch. 7, sec. 2, pp.272-287.
- [30] R. Bancroft, "Rectangular Microstrip Antennas," *Microstrip and Printed Antenna Design*, Atlanta: Noble Publishing Corporation, 2004, ch. 2, sec. 5, pp. 37-48.
- [31] G. Kumar and K.P. Ray, "An Introduction to Microstrip Antennas" *Broadband Microstrip Antennas*, Norwood: Artech House, Inc., 2003, ch. 1, sec.5, pp.11-18.
- [32] Z. N. Chen and M. Y. W. Chia, *Broadband Planar Antennas*, West Sussex: John Wiley & Sons Ltd., 2006.
- [33] M. Drakaki, A. Hatzopoulos, and A. Siskos, "CMOS Inductor Performance Estimation using Z- and S-parameters," *IEEE International Symposium on Circuits and Systems*, 2007, pp. 2256-2259, May 2007.
- [34] J. R. James and P.S. Hall, *Handbook of Microstrip Antennas*, vol. 1. London: Peter Peregrinus Ltd., 1989.
- [35] M.D. DuFault and A.K. Sharma, "A novel calibration verification procedure for millimeter-wave measurements," *IEEE MTT-S International Microwave Symposium Digest*, vol. 3, pp.1391-1394, Jun. 1996.

- [36] D.C. DeGroot, K.L. Reed, and J.A. Jargon, "Equivalent Circuit Models for Coaxial OSLT Standards," *54th ARFTG Conference Digest-Spring*, vol. 36, pp. 1-13, vol. 36, Dec. 2000.
- [37] D. Rytting. (1998, Sept.). Network Analyzer Error Models and Calibration Methods. Hewlett-Packard Company. [Online White Paper]. Available: <http://cpd.ogi.edu/IEEE-MTT-ED/Network%20Analyzer%20error%20Models%20and%20Calibration%20Methods.pdf>
- [38] D.M. Jamal and T.A. Fieldly, *CMOS RF Modeling, Characterization and Applications*, Singapore: World Scientific Publishing, 2002.